Average pCO₂ fell but river-forming climates persisted on Mars 3.6-3 Ga

Authors: Edwin S. Kite[1,*], Michael A. Mischna[2], Alexander M. Morgan[3,4], Sharon A. Wilson[3], Mark I. Richardson[5].

Affiliations:

[1]University of Chicago, Chicago, IL.

[2]Jet Propulsion Laboratory, Caltech, Pasadena, CA.

[3]Smithsonian Institution, Washington, DC.

[4]Planetary Science Institute, Tucson, AZ.

[5]Aeolis Research, Chandler, AZ.

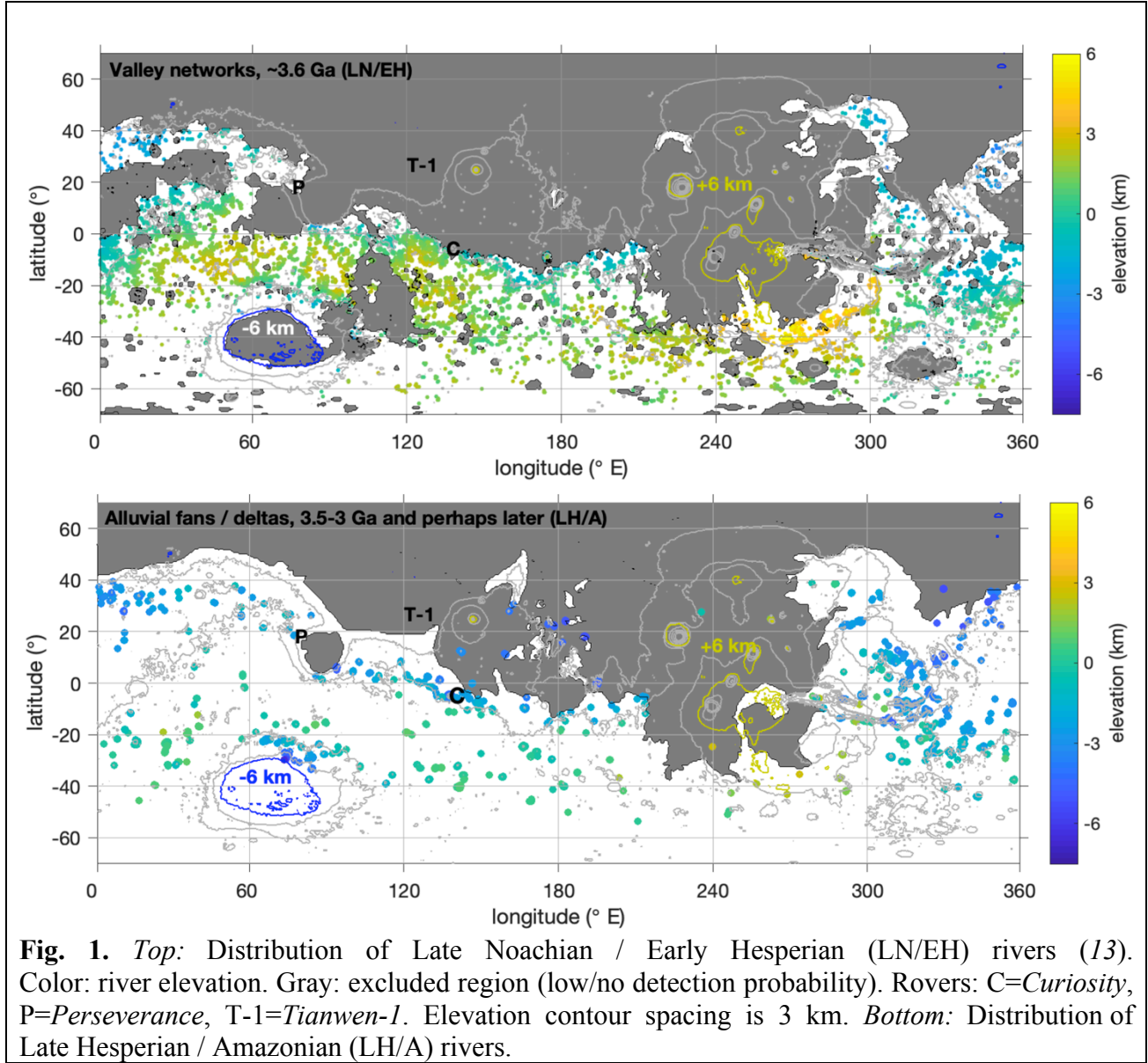*Correspondence to: kite@uchicago.edu

Abstract: Mars' river valleys are dry today, and the planet has lost most of its initial atmospheric volatiles; however it remains unclear whether river-forming climates required high pCO_2 (≈atmospheric pressure). Atmospheric pressure affects the spatial distribution of climate-sensitive landforms on Mars. We find evidence in the detectability-corrected paleoriver distributions for changes over time in the spatial distribution of rivers – a decline in the preferred elevation for rivers, and a shift from early-stage elevation control to late-stage latitude control. Both are well-explained by a reduction in the total strength of the atmospheric greenhouse effect, with a decline in average pCO_2 from $\gg 10^2$ mbar for early river-forming climates, to $\lesssim 10^2$ mbar for later river-forming climates. River-forming climates at low average pCO_2 on Mars challenge Habitable Zone theory.

One Sentence Summary: Changes over time in the latitude and altitude distribution of water flow on Mars indicate that pCO_2 had already declined before the end of Mars' river-forming era.

Main Text: Mars is the only world whose surface is known to have become uninhabitable. The surface today is a cold desert, but the climate 3.6-3 Ga was at least intermittently warm enough for rivers and long-lived lakes (inferred to have been habitable) (e.g., *1-3*). Today Mars' total atmospheric pressure (CO_2-dominated, ~6 mbar) is close to the triple point of water, so higher pCO_2 was probably needed for lakes. Some atmosphere has been lost by escape-to-space (*4*), and Mars should have formed with the capacity to outgas many bars of CO_2 (on Mars, $pCO_2 \approx$ total atmospheric pressure) (*5*). However, little is known about the evolution of pCO_2 over geologic time (*6*, and references therein). CO_2 is the most important climate-regulating greenhouse gas in the modern Solar System. Building on this fact, the Habitable Zone (HZ) concept (*7*) predicts that if worlds near the cold edge of the HZ (such as Early Mars) are habitable, then they should have $\gtrsim 1$ bar pCO_2. The prevailing view is that $pCO_2 \gtrsim 1$ bar was necessary (though insufficient) for past Mars habitability (*5*). Here, we test and reject this hypothesis using geologic proxies for past river activity and past average pCO_2 that time-resolve Mars' desertification.

Mars' geology records multiple eras of precipitation-fed water runoff (e.g., *3, 6*) (Fig. S1). Regionally integrated Valley Networks (VNs) formed early, ~3.6 Ga (*8*). Later, 3.5-3 Ga

50   (and perhaps later), multiple river-forming climates created deltas and alluvial fans (e.g., *2-3*; SM), with a very different spatial distribution from the VNs (Fig. 1). (We exclude rivers not formed by precipitation, e.g., associated with geothermal heating, groundwater outbursts, and localized impact-induced effects, as well as young gullies; SM). Here we use the changes over time in the spatial distribution of precipitation-fed rivers/lakes (Fig. 1) to probe past changes in pCO$_2$ and the

55   strength of the atmospheric greenhouse effect.

Fig. 1. *Top:* Distribution of Late Noachian / Early Hesperian (LN/EH) rivers (*13*). Color: river elevation. Gray: excluded region (low/no detection probability). Rovers: C=*Curiosity*, P=*Perseverance*, T-1=*Tianwen-1*. Elevation contour spacing is 3 km. *Bottom:* Distribution of Late Hesperian / Amazonian (LH/A) rivers.

Models predict that the spatial distribution of Mars water runoff depends on pCO$_2$. For pCO$_2 \gg 10^2$ mbar, models predict that surface temperature (T_{surf}) falls with elevation following the

60   atmospheric adiabatic lapse rate, so (as on Earth) high ground acts as a cold trap for snow and ice (*9*). (Mars' topography has a range and standard deviation 3.5× greater than Earth's.) On a planetary surface that had only (3±2)% of Earth's area-averaged H$_2$O abundance (*10*), cold-trapped high-elevation snow/ice is a water source for runoff during melt events (*9*). By contrast, for pCO$_2 \lesssim 10^2$ mbar, the CO$_2$ greenhouse effect is much weaker, and insolation dominates surface

65   energy balance. As a result, there is strong latitude (i.e., insolation) control for T_{surf} and for

2

snow/ice distribution, with low-elevation snow/ice accumulation possible (e.g., *11*). This prediction matches data for <1.5 Ga geologic features (*12*). Given its potential as a probe of the ancient greenhouse effect and pCO_2, it is perhaps surprising that Mars' paleo-river distribution has not previously been analyzed for latitude/elevation trends with correction for detectability biases.

70

We analyze a late-stage rivers database, and an existing Valley Networks database (*13*), correcting both, for the first time, for postfluvial resurfacing (i.e., detectability/preservation bias; SM). The late-stage rivers database was compiled by systematically searching for fan-shaped deposits between 90°N and 90°S using globally-available Context Camera (CTX) images (SM). Although
75   data poleward of 40° or below -6 km (dotted lines in Fig. 2) are likely further biased to lower frequency by postfluvial resurfacing, this does not affect the trends reported here. VNs formed preferentially at high elevation (Fig. 2) (contrary to uncorrected catalogs, Fig. S2a). VN-era climate was thus warm enough for runoff at high elevations at least intermittently and there was a source of water (snow, ice, or rain) at high elevations (*9*). If pCO_2 was high when the VNs
80   formed, as strongly suggested by their elevation and relatively weak latitude preferences (*9*), then low-elevation, equatorial temperatures exceeded 290 K. The VN-era atmospheric greenhouse effect was very strong.
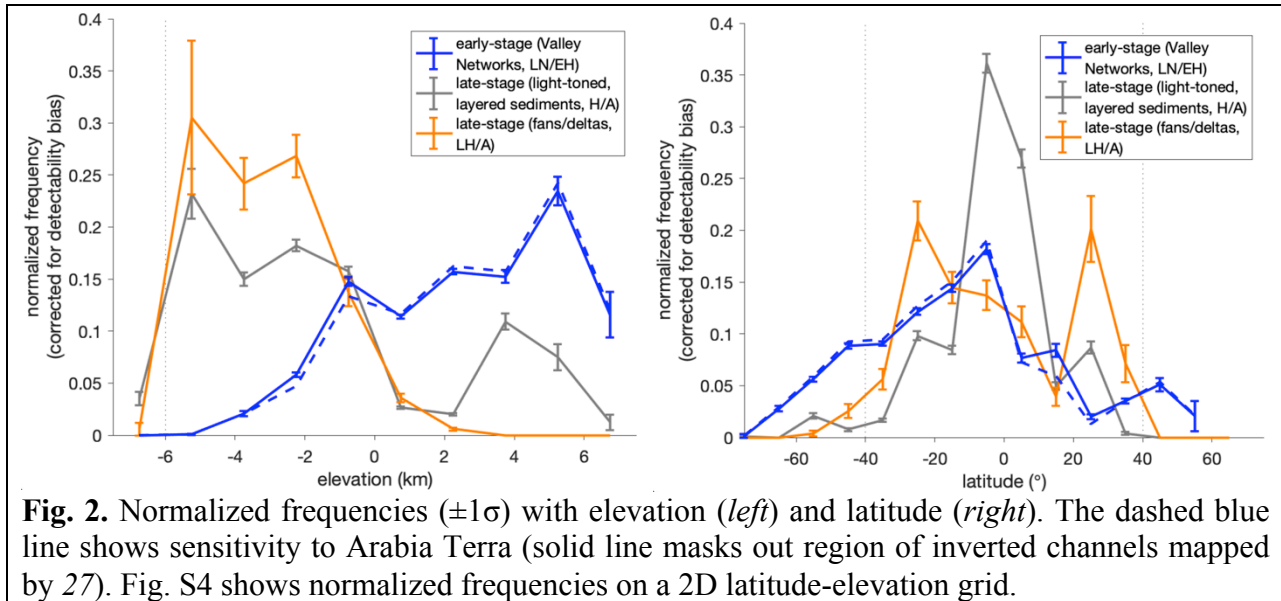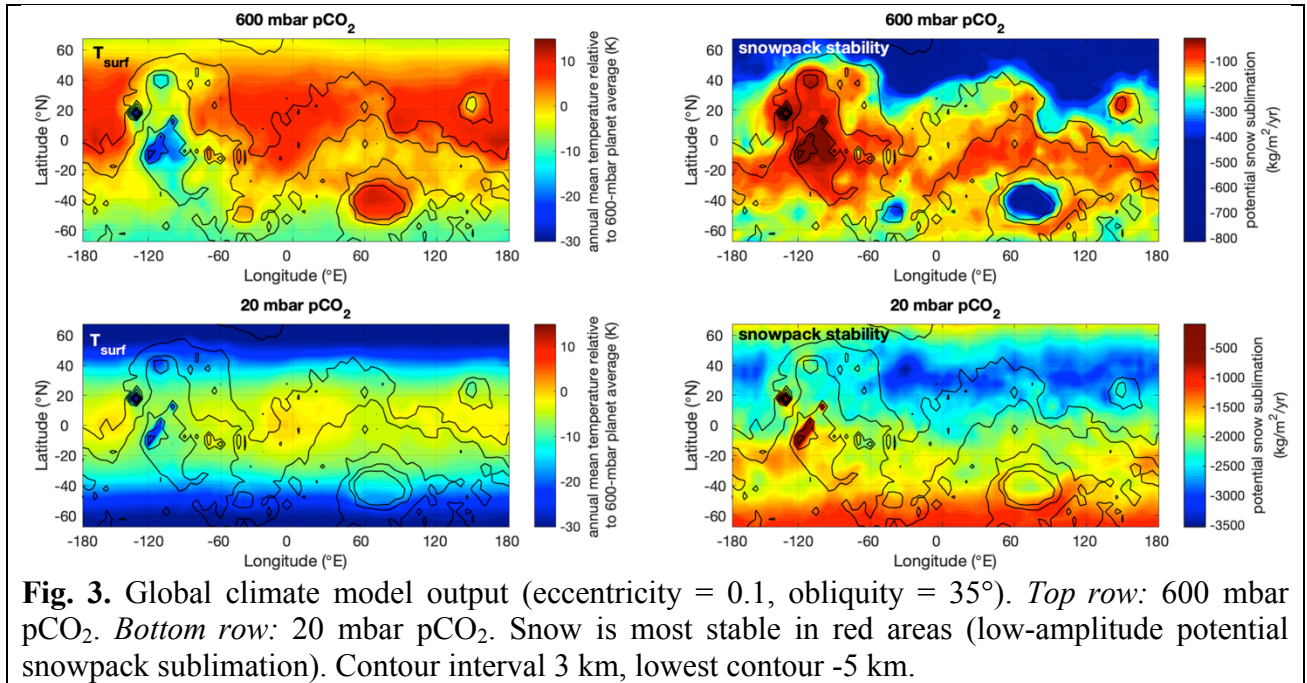

Fig. 2. Normalized frequencies (±1σ) with elevation (*left*) and latitude (*right*). The dashed blue line shows sensitivity to Arabia Terra (solid line masks out region of inverted channels mapped by *27*). Fig. S4 shows normalized frequencies on a 2D latitude-elevation grid.

85   Relative to early-stage rivers, rivers later in Mars history formed preferentially at lower elevations, and were more tightly collimated by latitude (Fig. 2). The global low-elevation preference reflects local processes, as late-stage rivers mostly flowed within <200-km sized topographic catchments. The decline in river-elevation preferences over time (Fig. 2a) is not sensitive to how river elevation is measured (Figs. S2-S3). The decline is consistent with a waning greenhouse effect,
90   such that at high elevation, late-stage temperatures stayed below freezing. Considering the strong late-stage latitude control (Fig. 2b), e.g., the southern midlatitude band of intermediate-elevation fans (Fig. 1b), the change over time in the river distribution is inconsistent with a switch from a precipitation to a groundwater source for river water. Late-stage rivers have headwaters on local high ground, and in many cases also regional high ground, which argues against groundwater
95   discharge (SM). Groundwater might still play an important role in setting lake levels. Latitude control is not an artifact of latitude-dependent hypsometry (Fig. S4). The distribution of (post-VN) light-toned layered sedimentary rocks is consistent with these trends (Fig. 2, Figs. S4-S5). The broadly symmetric distribution of late-stage rivers across the equator does not support (nor

disprove) the putative existence of a late-stage northern-hemisphere ocean. All these data
are simply explained if late-stage river-forming climates (and thus a hydrologic cycle) occurred at
$\lesssim 10^2$ mbar pCO_2. Alternatively, these data might be explained if Mars repeatedly transitioned
from a subfreezing, low-pCO_2 climate to a warm, high-pCO_2 climate on timescales so fast
($\sim 10^3$ yr) that snow/ice accumulations at locations in equilibrium with low-pCO_2 climate had
insufficient time to sublimate away, and instead melted in place. Low total pCO_2 is necessary for
atmosphere collapse-inflation cycles (*14*). In either case, average pCO_2 fell 3.6-3 Ga but river-
forming climates persisted.

We neglect postfluvial tectonics, which was likely minor (SM). Post-valley-network True Polar
Wander (TPW) has been claimed using indirect geologic proxies (*15*) but these are affected by
resurfacing biases (Fig. S6) and other effects. If post-valley-network TPW was, in fact, ~20°, then
our conclusion that VNs formed at high elevation (Fig. 2a) would be unaffected. Wiggling of the
southern midlatitude band of late-stage rivers is well explained by coupling between atmospheric
water transport and ancient topography, without TPW (SM).

Fig. 3. Global climate model output (eccentricity = 0.1, obliquity = 35°). *Top row:* 600 mbar
pCO_2. *Bottom row:* 20 mbar pCO_2. Snow is most stable in red areas (low-amplitude potential
snowpack sublimation). Contour interval 3 km, lowest contour -5 km.

Precipitation-fed runoff requires temperatures above freezing and a source of H_2O (rain or
snowpack). To confirm that spatial patterns of T_{surf} and snow/ice stability depend on pCO_2 (*9*),
we used the MarsWRF global climate model (GCM) (*16-17*) (SM). CO_2 greenhouse warming is
insufficient to explain ancient rivers on Mars (e.g., *9*). Our model does not include the unknown
non-CO_2 greenhouse-warming agent, but in order to provide the needed warming all proposed
non-CO_2 greenhouse-warming agents contribute little to total pressure, and are fairly well-mixed
horizontally; therefore the effects of pCO_2 shown here should be robust. Although paleo-river
distributions almost certainly record multiple orbital states, the basic trend of latitude control
versus elevation control is robust to this uncertainty. At 600 mbar pCO_2, snow is most stable on
high ground, and the temperature dependence on latitude is less pronounced (Fig. 3, Figs. S7-S9).
This pattern is consistent with the high-elevation preference and modest latitudinal control for
early-stage rivers (Fig. 4). 20-mbar pCO_2 output is much colder, with strong latitudinal banding in
T_{surf} pack stability, and a gentle trend to higher temperatures at lower elevation (Fig. 3,

Figs. S7-S11). This is consistent with the observed distribution of late-stage rivers (Figs. 1-2).
130 (60 mbar simulations show an intermediate pattern; Fig. S10). The lack of high-elevation late-stage rivers indicates a weaker total greenhouse effect at later times, so that high-elevation precipitation stayed frozen. Overall, data-model comparison shows that changes over time in the distribution of Mars paleo-rivers in space (Figs. 1-2) are consistent with expectations for Mars' long-term atmospheric evolution – i.e., a decline in Mars pCO_2 and a weakening of Mars'
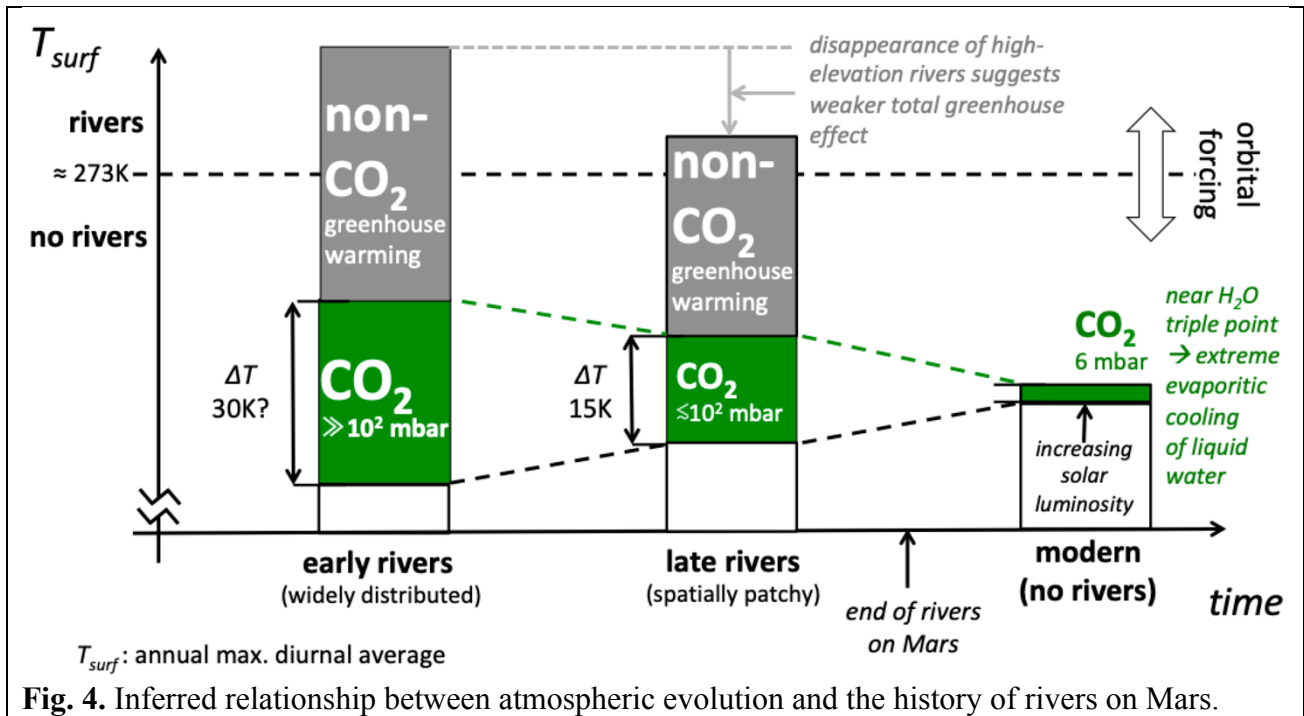135 atmospheric greenhouse effect (Fig. 3, Figs. S10-S12).

If the late-stage rivers were caused by multiple individually brief (<10 yr-duration) atmospheric heating transients (for example, with energy for runoff ultimately sourced from impacts), then sustained strong non-CO_2 greenhouse warming would not be required to explain late-stage rivers.
140 This brief-heating hypothesis fails to explain data at some localities (e.g., *2*). We found that brief-heating also fails at a global scale (Figs. S13-S17). Specifically, we surveyed 212 large, young impact craters (from *18*); almost all are closed basins. Within these craters, we found 12 prefluvial/synfluvial impact craters. To form these prefluvial/synfluvial craters requires a ≥0.2 Gyr wait time (Table S1), far too long for river formation by localized impact-induced effects
145 (consistent with ref. *19*). Within large, young impact craters, we surveyed constraints on late-stage lake area, A, and topographic catchment area, D (finding $n = 118$ basins with useful constraints). $D/A − 1$ (equal to the hydrologic X-ratio, X_H; *20*) is approximately equal in closed-basin hydrological steady state to the Aridity Index (AI) (ratio of potential evaporation to water discharge, neglecting runoff production on the lake and net of infiltration). Brief wet climates
150 predict higher X_H for bigger craters ($X_H \propto R_{crater}^{2/3}$) because small sinks fill quicker than big sinks (SM). We observe the opposite global trend (Fig. S15a), with $X_H<10$ found mainly in large craters. This disfavors the scenario in which late-stage river-forming climates were powered by the greenhouse forcing from a single volcanic eruption, or the energy of a distant impact. Additional trends in aridity data further support relatively long-lived late-stage river-forming
155 climates (Fig. S15). Most of the fluvial sediment transport was driven by runoff from crater sidewalls. Lake levels could also have been maintained by water conveyed from crater sidewalls (by overland flow or shallow groundwater flow) or alternatively, by deep-sourced groundwater sourced from rain/melt recharge at ~10^2-10^3-km scales (e.g. *21*) (a spatial footprint that is a small number of pixels in our GCM). Overall, the results of our global survey provide quantitative
160 support for the inference (e.g., *2*) that an arid but essentially Earth-like hydrologic cycle fueled late-stage rivers. Sustained strong non-CO_2 climatic greenhouse warming is required.

Sustained strong non-CO_2 greenhouse forcing for late-stage river-forming climates cannot be explained by H_2 degassing following impacts (*22*); multiple hypotheses remain viable (*6*),
165 for example H_2 released from the planet's interior, or high-altitude water ice clouds. The triggers for the river-forming climates are also unknown (one possibility is volatile release associated with groundwater discharge). The *Perseverance* rover can test hypotheses in situ. For example, detrital siderite would favor moderate river pH and thus low pCO_2.

170 Low average pCO_2 3.5-3 Ga is consistent with isotopic evidence that most of Mars' atmosphere was lost >3.5 Ga (e.g., *23*). Candidate carbon sinks include escape-to-space, carbonate formation, and basal melting of CO_2 ice. Alternatively, CO_2 could have been reversibly sequestered as CO_2 ice.

175 The inventory of H_2O at or near Mars' surface has apparently decreased three-fold since 3.5 Ga (*24*). H_2O loss does not fully explain changes in river distribution (e.g., mid-elevation rivers at ~25°S; Fig. 1b), but H_2O loss likely contributed to the observed changes. For example, if crustal

5

pore space became desiccated, then during very warm climates meltwater/rain could trickle down into the subsurface, drying out the surface. The end of river-forming climates on Mars could have been caused by further H_2O loss, further C loss, or a reduction in non-CO_2 greenhouse warming (Fig. 4).

Fig. 4. Inferred relationship between atmospheric evolution and the history of rivers on Mars.

Searches for habitable exoplanets are guided by the Habitable Zone (HZ) concept (*7*). This concept predicts that habitable worlds near the cold edge of the HZ should have high pCO_2 (*25*). However, we find that Mars (near the cold edge of the HZ) had river-forming climates at low average pCO_2. This raises the likelihood of false negatives in the search for habitable exoplanets. So far, rocky exoplanet atmosphere detection (*26*) has used methods that do not reliably detect ~10^2 mbar atmospheres. At ~10^2 mbar average atmospheric pressure, Mars had a surface climate that was habitable, at least intermittently. Therefore non-detection of an atmosphere on an exoplanet does not preclude its habitability.

In summary, changes over time in the spatial pattern of paleochannels on Mars suggest declining average atmospheric pressure and a waning greenhouse effect. Mars' average atmospheric pressure fell below Earth-like levels too early for this to explain why Mars' river-forming climates ceased. If pCO_2 was $\lesssim 10^2$ mbar when rivers flowed, then high levels of pCO_2 are not only insufficient but also unnecessary to explain rivers, widening the gap between data and Mars paleoclimate models. However, a further decline in pCO_2 remains a possible explanation for the cessation of river-forming climates on Mars. Our results suggest that surface lakes and rivers can be generated by a broader range of planetary climate states than previously thought.

References and Notes:

1. Grotzinger, J. P.; Sumner, D. Y.; Kah, L. C.; Stack, K.; Gupta, S.; Edgar, L.; Rubin, D.; Lewis, K.; Schieber, J.; Mangold, N.; Milliken, R.; et al., 2014, A Habitable Fluvio-Lacustrine Environment at Yellowknife Bay, Gale crater, Mars, Science, 343,6169, id. 1242777 (2014).

2. Irwin, R.P., K.W. Lewis, A.D. Howard, J.A. Grant, Paleohydrology of Eberswalde crater, Mars. Geomorphology, https://doi.org/10.1016/j.geomorph.2014.10.012 (2015)

210

3. Grant, J.A.; Wilson, S.A., Late alluvial fan formation in southern Margaritifer Terra, Mars, Geophys. Res. Lett., 38, CiteID L08201 (2011).

4. Jakosky, B.M., Brain, D., Chaffin, M., Curry, S., Deighan, J., Grebowsky, J., Halekas, J., Leblanc, F.,
215   Lillis, R., Luhmann, J.G., et al., Loss of the Martian atmosphere to space: present-day loss rates determined from MAVEN observations and integrated loss through time. Icarus 315, 146-157 (2018).

5. Haberle, R. M.; Catling, D. C.; Carr, M. H.; Zahnle, K. J., The Early Mars Climate System, in The atmosphere and climate of Mars, R.M. Haberle et al. (Eds.), Cambridge University Press, 497-525
220   (2017).

6. Kite, E.S., Geologic constraints on Early Mars climate, Space Science Reviews, 215:10 (2019).

7. Kopparapu, R. K.; Ramirez, R.; Kasting, J. F.; Eymet, V.; Robinson, T. D.; Mahadevan, S.; et al.,
225   Habitable Zones around Main-sequence Stars: New Estimates, Astrophysical Journal, 765, 131 (2013).

8. Fassett, C. I.; Head, J. W., The timing of martian valley network activity: Constraints from buffered crater counting, Icarus,195, 61-89 (2008).

230   9. Wordsworth, R., The Climate of Early Mars, Ann. Rev. Earth Planet. Sci., 44, 381-408 (2016).

10. Alsaeed, N. R.; Jakosky, B. M., Mars Water and D/H Evolution From 3.3 Ga to Present, J. Geophys. Res.: Planets, 124, 3344-3353 (2019).

235   11. Madeleine, J.-B. et al., Amazonian northern mid-latitude glaciation on Mars: A proposed climate scenario. Icarus 203, 390–40 (2009).

12. Fassett, C.I., Dickson, J.L., Head, J.W., Levy, J.S., and Marchant, D.R., Supraglacial and proglacial valleys on Amazonian Mars. Icarus 208, 86–100 (2010).
240

13. Hynek, B. M.; Beach, M.; Hoke, M. R. T., Updated global map of Martian valley networks and implications for climate and hydrologic processes, J. Geophys. Res.,115,E9, E09008 (2010).

14. Forget, F.; R. Wordsworth, E. Millour, J.-B. Madeleine, L. Kerber, J. Leconte, E. Marcq, R.M. Haberle,
245   3D modelling of the early Martian climate under a denser CO_2 atmosphere: temperatures and CO_2 ice clouds. Icarus 222, 81–99 (2013).

15. Bouley, S., et al., Late Tharsis formation and implications for early Mars, Nature, 531, 344-347 (2016).

250   16. Richardson, M.I.; Toigo, A.D.; Newman, C.E., Investigation of the nature and stability of the Martian seasonal water cycle with a general circulation model, J. Geophys. Res., 112, E09001 (2007).

17. Toigo A.D., C. Lee, C.E. Newman, M.I. Richardson, The impact of resolution on the dynamics of the Martian global atmosphere: Varying resolution studies with the MarsWRF GCM, Icarus 221, 276-288
255   (2012).

18. Tanaka, K.L., Skinner, J.A., Jr., Dohm, J.M., Irwin, R.P., III, Kolb, E.J., Fortezzo, C.M., Platz, T., Michael, G.G., and Hare, T.M., Geologic map of Mars: USGS Scientific Investigations Map 3292 (2014).

260   19. Kite, E. S.; Sneed, J.; Mayer, D. P.; Wilson, S.A., Persistent or repeated surface habitability on Mars during the late Hesperian – Amazonian, Geophys. Res. Lett., 44, 3991-3999 (2017).

20. Matsubara, Y.; Howard, A. D.; Drummond, S.A., Hydrology of early Mars: Lake basins, J. Geophys. Res.,116,E4, E04001 (2011).
265

21. Horvath, D. G.; Andrews-Hanna, J. C., Reconstructing the past climate at Gale crater, Mars, from hydrological modeling of late-stage lakes, Geophys. Res. Lett., 44, 8196-8204 (2017).

22. Haberle, R.M., et al., Impact Degassing of H_2 on Early Mars and its Effect on the Climate System,
270   Geophys. Res. Lett., 46(22),13355-13362 (2019).

23. Webster, C. R.; Mahaffy, R.; Flesch, G.J.; et al., Isotope Ratios of H, C, and O in CO_2 and H_2O of the Martian Atmosphere, Science, 341, 260-263 (2013).

275   24. Mahaffy, R.; Webster, C. R.; Stern, J. C.; et al., The imprint of atmospheric evolution in the D/H of Hesperian clay minerals on Mars, Science, 347, 6220, 412-414 (2015).

25. Bean, J.L., Abbot, D., and Kempton, E. M-R., A Statistical Comparative Planetology Approach to the Hunt for Habitable Exoplanets and Life Beyond the Solar System, Astrophys. J. Lett., 841:L24 (2017).
280

26. Kreidberg, L., et al. Absence of a thick atmosphere on the terrestrial exoplanet LHS 3844b, Nature, 573, 87-90 (2019).

27. Davis, J. M., Balme, M., Grindrod, P. M., Williams, R. M. E., Gupta, S., Extensive Noachian fluvial
285   systems in Arabia Terra: Implications for early Martian climate. Geology 44, 847–850 (2016).

28. Malin, M.C., K.S. Edgett, Evidence for persistent flow and aqueous sedimentation on early Mars. Science 302(5652), 1931–1934 (2003).

290   29. Ehlmann, B.L. & C.S. Edwards, Mineralogy of the Martian surface. Annu. Rev. Earth Planet. Sci. 42(1), 291–315 (2014).

30. Burr, D.M., P.A. Carling, V.R. Baker, Megaflooding on Earth and Mars (Cambridge University Press, Cambridge) (2009).
295

31. Kraal, E.R., M. van Dijk, G. Postma, M.G. Kleinhans, Martian stepped-delta formation by rapid water release. Nature 451(7181), 973–976 (2008).

32. Lapôtre, M.G.A., M.P. Lamb, Substrate controls on valley formation by groundwater on Earth and
300   Mars. Geology 46(6), 531–534 (2018).

33. Hauber, E. et al. Asynchronous formation of Hesperian and Amazonian-aged deltas on Mars and implications for climate. J. Geophys. Res. 118, 1529–1544 (2013)

305   34. Malin, M.C., K.S. Edgett, B.A. Cantor, M.A. Caplinger, G.E. Danielson, E.H. Jensen, M.A. Ravine, J.L., et al., An overview of the 1985–2006 Mars Orbiter Camera science investigation. Mars J. 5, 1–60 Mars Int. J. Mars Sci. Explor. 4, 1–60 (2010).

35. Irwin, R.P., Testing links between impacts and fluvial erosion on post-Noachian Mars, in 44th Lunar
310   and Planetary Science Conference, The Woodlands, Texas. LPI Contribution, vol. 1719, p. 2958 (2013).

36. Barnhart, C.J.; Nimmo, F. Travis, B.J., Martian post-impact hydrothermal systems incorporating freezing, Icarus, Volume 208, 101-117 (2010).

315 37. Steakley, Kathryn; Murphy, James; Kahre, Melinda; Haberle, Robert; Kling, Alexandre, Testing the impact heating hypothesis for early Mars with a 3-D global climate model, Icarus, 330, 169-188 (2019).

38. Turbet, M.; Gillmann, C.; Forget, F.; Baudin, B.; Palumbo, A.; Head, J.; Karatekin, O., The environmental effects of very large bolide impacts on early Mars explored with a hierarchy of 320 numerical models, Icarus, 335, article id. 113419 (2020)

39. Morgan, A.M., S.A. Wilson, A.D. Howard, R.A. Craddock, J.A. Grant, Global distribution of alluvial fans and deltas on Mars, in 49th Lunar and Planetary Science Conference, The Woodlands, Texas. LPI Contribution, vol. 2083, 2219 (2018).

325

40. Goddard, K., N.H. Warner, S. Gupta, J.-R. Kim, Mechanisms and timescales of fluvial activity at Mojave and other young Martian craters. J. Geophys. Res., Planets 119(3), 604–634 (2014).

41. Weiss, D.K., & J.W. Head, Extensive Amazonian-aged fluvial channels on Mars: Evaluating the role of 330 Lyot crater in their formation, Geophys. Res. Lett., 44, 5336-5344 (2017).

42. Dundas, C.M. , A.S. McEwen, S. Diniega, C.J. Hansen, S. Byrne, J.N. McElwaine, The Formation of Gullies on Mars Today. pp. 67-94 in S.J. Conway et al. (eds.), Martian Gullies & Their Earth Analogs, Special Publications, vol. 467, Geological Society, London (2017).

335

43. Squyres, S.W.; Kasting, J.F., Early Mars: How Warm and How Wet?, Science, 265, 744-749 (1994).

44. Fassett, C., & J.W. Head, Valley formation on martian volcanoes in the Hesperian: Evidence for melting of summit snowpack, caldera lake formation, drainage and erosion on Ceraunius Tholus, Icarus, 340 189, 118-135 (2007).

45. Kite, E.S., Mayer, D.P., Wilson, S., Davis, J., Lucas, A.S., & Stucky de Quay, G., Persistence of Intense, Climate-Driven Runoff Late in Mars History, Science Advances, 5(3), eaav7710 (2019).

345 46. Palucis, M. C.; Jasper, J.; Garczynski, B.; Dietrich, W. E., Quantitative assessment of uncertainties in modeled crater retention ages on Mars, Icarus, 341, article id. 113623 (2020).

47. Milliken, R.E., R.C. Ewing, W.W. Fischer, J. Hurowitz, Wind-blown sandstones cemented by sulfate and clay minerals in Gale Crater, Mars. Geophys. Res. Lett. 41(4), 1149–1154 (2014).

350

48. Mangold, M., Dromart, G., Ansan, V., Salese, F., Kleinhans, M.G., Masse´, M., Quantin, C., and Stack, K.M. Fluvial regimes, morphometry, and age of Jezero crater paleolake inlet valleys and their exobiological significance for the 2020 Rover Mission Landing Site. Astrobiology 20:994–1013 (2020).

355 49. Michael, G.G. Planetary surface dating from crater size-frequency distribution measurements: multiple resurfacing episodes and differential isochron fitting. Icarus 226(1), 885–890 (2013).

50. Alemanno, G., Orofino, V., & Mancarella, F. Global map of Martian fluvial systems: Age and total eroded volume estimations. Earth & Space Science, 5, 560–577 (2018).
360

51. Luo, W., X. Cang, A.D. Howard, New Martian valley network estimate consistent with ancient ocean and warm and wet climate. Nat. Commun. 8, 15766 (2017).

52. Kraal, E.R., E. Asphaug, J.M. Moore, A. Howard, A. Bredt, Catalogue of large alluvial fans in Martian impact craters. Icarus 194(1), 101–110 (2008).

53. Nimmo, F.; Tanaka, K., Early Crustal Evolution of Mars, Ann. Rev. Earth Planet. Sci., 33, 133-161 (2005).

54. Smith, D.E., M.T. Zuber, H.V. Frey, J.B. Garvin, J.W. Head, D.O. Muhleman, G.H. Pettengill, R.J. Phillips, Solomon, S.C., H.J. Zwally, W.B. Banerdt, T.C. Duxbury, M.P. Golombek, F.G. Lemoine, G.A. Neumann, D.D. Rowlands, O. Aharonson, P.G. Ford, A.B. Ivanov, C.L. Johnson, P.J. McGovern, J.B. Abshire, R.S. Afzal, X. Sun, Mars orbiter laser altimeter: experiment summary after the first year of global mapping of Mars. J. Geophys. Res. 106(E10), 23689–23722 (2001).

55. Kreslavsky, M.A., Head, J.W., Mars climate history: insights from impact crater wall slope statistics. Geophys. Res. Lett. 45, 1751–1758 (2018).

56. Williams, Rebecca M. E.; Phillips, Roger J., Morphometric measurements of martian valley networks from Mars Orbiter Laser Altimeter (MOLA) data, J. Geophys. Res., 106, 23737-23752 (2001).

57. Grimm, R. E.; Solomon, S. C., Tectonic tests of proposed polar wander paths for Mars and the Moon, Icarus, Volume 65, Issue 1, p. 110-121 (1986).

58. Citron, R.I., M. Manga, D.J. Hemingway, Timing of oceans on Mars from shoreline deformation. Nature 555(7698), 643–646 (2018).

59. Sholes, S.F.; Montgomery, D.R.; Catling, D.C., Quantitative High-Resolution Reexamination of a Hypothesized Ocean Shoreline in Cydonia Mensae on Mars, J. Geopys. Res. - Planets, 124, 316-336 (2019).

60. Scanlon, K. E.; Head, J. W.; Fastook, J. L.; Wordsworth, R. D., The Dorsa Argentea Formation and the Noachian-Hesperian climate transition, Icarus, 299, 339-363 (2018).

61. Holo, S.J., Kite, E.S., & Robbins, S.J., Mars obliquity history constrained by elliptic crater orientations, Earth & Planetary Science Letters, 496, 206-214. (2018).

62. Beyer, R., K. Stack, J.L. Griffes, R.E. Milliken, K.E. Herkenhoff, S. Byrne, J.W. Holt, J.P. Grotzinger An atlas of Mars sedimentary rocks as seen by HiRISE, in Sedimentary Geology of Mars, eds. JP Grotzinger and RE Milliken, SEPM Special Publication No. 102 (2012).

63. Mischna, M.A.; Lee, C.; Richardson, M., Development of a fast, accurate radiative transfer model for the Martian atmosphere, past and present, J. Geophys. Res., 117, E10009 (2012).

64. Mischna, M. A.; Baker, V.; Milliken, R.; Richardson, M.; Lee, C., Effects of obliquity and water vapor/trace gas greenhouses in the early martian climate, J. Geophys. Res.: Planets,118,3, 560-576 (2013).

65. R.D. Wordsworth, L. Kerber, R.T. Pierrehumbert, F. Forget, J.W. Head, Comparison of "warm and wet" and "cold and icy" scenarios for early Mars in a 3-D climate model. J. Geophys. Res., Planets 120(6), 1201–1219 (2015).

66. Salese, F.; Pondrelli, M.; Neeseman, A.; Schmidt, G.; Ori, G. G., Geological Evidence of Planet-Wide Groundwater System on Mars, J. Geophys. Res. - Planets, 124, 374-395 (2019).

415   67. Malin, M.C.; Bell, J.F.; Cantor, B.A.; Caplinger, M.A.; Calvin, W.M.; Clancy, R. T.; Edgett, K.S., et al., Context Camera Investigation on board the Mars Reconnaissance Orbiter, J. Geophys. Res., 112(E5), CiteID E05S04 (2007).

        68. McEwen, A.S., E.M. Eliason, J.W. Bergstrom, N.T. Bridges, C.J. Hansen, W.A. Delamere, J.A. Grant,
420   V.C. Gulick, K.E. Herkenhoff, L. Keszthelyi, R.L. Kirk, M.T. Mellon, S.W. Squyres, N. Thomas, C.M. Weitz, Mars Reconnaissance Orbiter's High Resolution Imaging Science Experiment (HiRISE). J. Geophys. Res. 112, E5, E05S02 (2007).

        69. Moore, J. M.; Howard, A. D., Large alluvial fans on Mars, J. Geophys. Res. - Planets 110(E4), CiteID
425   E04005 (2005).

        70. J.A. Grant, R.P. Irwin III, J.P. Grotzinger et al., HiRISE imaging of impact megabreccia and sub-meter aqueous strata in Holden Crater, Mars. Geology 36, 195–198 (2008).

430   71. Davis, J.M.; Gupta, S.; Balme, M.; Grindrod, P.M.; Fawdon, P.; Dickeson, Z.I.; Williams, R. M. E., A Diverse Array of Fluvial Depositional Systems in Arabia Terra: Evidence for mid-Noachian to Early Hesperian Rivers on Mars, J. Geophys. Res.: Planets, 124, 1913-1934 (2019).

        72. Palucis, M.C., W.E. Dietrich, R.M.E. Williams, A.G. Hayes, T. Parker, D.Y. Sumner, N. Mangold,
435   K. Lewis, H. Newsom, Sequence and relative timing of large lakes in Gale Crater (Mars) after the formation of Mount Sharp. J. Geophys. Res., Planets 121(3), 472–496 (2016)

Supplementary Materials:

Materials and Methods

450   Figures S1-S18

Table S1

References (*28-72*)

455

Supplementary Materials for

460

Average pCO₂ fell but river-forming climates persisted on Mars 3.6-3 Ga

Edwin S. Kite, Michael A. Mischna, Alexander M. Morgan, Sharon A. Wilson,
Mark I. Richardson.

465

Corresponding author: Email: kite@uchicago.edu

This PDF file includes:

470

Supplementary Text (Materials and Methods)

Figs. S1 to S18

475   Table S1

Materials and Methods

1. Geologic background.

480   Early Mars had rivers and lakes (e.g., *1, 28*) (Fig. S1). Aqueous minerals (e.g. *29*) show that H_2O filled the lakes. In this study, we use rivers that were fed by precipitation (rain and/or meltwater). We omit channels that were formed by catastrophic outbursts of subsurface water (e.g., *30*) and we omit almost all features where there are arguments both for and against a groundwater origin (e.g., *31-32*). We do interpret as precipitation-fed a small number of deltas that were interpreted by

485   ref. *33* as formed by groundwater discharge. However, our results are robust to excluding all deltas, so this difference in interpretation is not important for our conclusions.

    We review the evidence that Mars had precipitation-fed rivers (e.g., *6,* and references therein). On Mars, the channel heads for young rivers can in many locations be traced up to ridgelines

490   (e.g., at 24.1°S 28.2°E, 22.7°S 73.8°E, 21.4°S 67.3°E, and 19.9°S 32.7°W). This is as expected for precipitation-fed runoff. By contrast, groundwater springs do not occur at ridgelines, nor on regional highs. Drainage density at some sites is much higher than expected for spring-fed streams (*34*). We do not distinguish between shallow subsurface flow (within topographic catchments) and overland flow. Both are fed by precipitation (rain or snowmelt), and so have similar implications

495   for paleoclimate.

    River water was mostly not produced by the localized effects of asteroid impacts (e.g., *2, 35-38*). River/lake sediments found within large impact craters frequently contain smaller prefluvial/synfluvial impact craters. To allow enough time for these craters to accumulate requires

500   a time gap between the formation of the host craters and the end of river activity of ≥0.2 Gyr (e.g., Table S1; and ref. *19*). The lifetime of post-impact hydrothermal activity is very much shorter (<0.0005 Gyr; e.g. *36*), precluding post-impact hydrothermal activity as a source for river water. Furthermore, river activity was not caused by the direct energy input from the impacts that formed the river-hosting crater. Moreover, simulations of impact-induced precipitation predict

505   ≲1 yr-duration wet climates, too brief to match data for late-stage rivers and lakes (e.g., *37-38*). The N-S orientation preference that has been reported for late-stage fans (*39*) also supports insolation, and not impact energy, as the energy source for surface runoff. The strong latitude dependence of fan-hosting craters (Fig. 2b) further supports insolation-controlled alluvial fan formation. It remains possible that impacts indirectly triggered wet climates by activating a

510   mechanism that trapped sunlight energy (for example, through low-albedo impact ejecta; or by activating a hysteresis in the climate system; or by releasing H_2, *22*). Some steep (>10°) young (<1 Gya?) fans that are too small (<10 km^2, usually <1 km^2) to be included in the Fig. 1b survey did result from the localized effect of asteroid impacts (e.g. *40*). These steep, small fans are found inside pristine impact craters (*40*). Possible water sources for these fans include localized

515   precipitation or fall-back of wet ejecta. Moreover, some asteroid impacts on Mars triggered melting or release of subsurface fluids (e.g., *41*), but these are easily distinguished from landforms formed by precipitation-fed rivers. We also omit young gullies, which might be formed by mass wasting (for example, of CO_2-ice; *42*).

520   Intense geothermal heating (*43*), or lava, can melt ice, but high runoff production rates (e.g., *45*) rule out geothermal meltwater as the source of runoff. Lava deposits are not found in the locations where rivers and lakes are seen, with rare exceptions (e.g., *44*) that are excluded from our databases.

525   <u>Chronologic constraints:</u> Early-stage valley networks are distinguished from late-stage rivers on the basis of crosscutting relationships, crater densities, and the degree of preservation of crater

530

535

rims (e.g. *3*, *46*). Late-stage rivers were usually shorter, and late-stage crater rim erosion is more concentrated into alcoves (e.g., *69*). Later periods of river-forming climate show spatially more restricted fluvial erosion, and fewer aqueous minerals, but with high rates of peak runoff production (*6*, *29*, *45*). In many places an epoch of deep wind erosion stratigraphically separates early-stage rivers from late-stage rivers (e.g. *47*). Although it is generally straightforward to distinguish between VNs and late-stage rivers, detailed study of one VN indicates that it was incompletely reactivated during later wet events (upstream of Jezero; *48*). Late-stage rivers date from the Late Hesperian and Amazonian (e.g., *3*, *46*). The currently most widely used mapping between relative and absolute age (*49*), which is uncertain by up to ±1 Gyr, is Noachian epoch → pre-3.6 Ga, Hesperian epoch → 3.6-3.2 Ga, Amazonian epoch → post-3.2 Ga. Ref. *8* reports crater counts on VNs that are consistent with VN formation during a <0.2 Ga interval around the Noachian-Hesperian boundary.

540 **2. Detectability-corrected surveys for presence/absence of rivers.**

545

The valley network (VN) database (from 13) shown in Fig. 1a was compiled using Thermal Emission Imaging System (THEMIS) data. Global VN databases compiled using higher-resolution image mosaics (*50*) and generated using Mars Orbiter Laser Altimeter (MOLA) data (*51*) show the same VN spatial distribution pattern, with only minor differences.

550

555

560

Our new fans/deltas database (Fig. 1b) was compiled by systematically searching for fan-shaped deposits between 90° N and 90° S using globally-available Context Camera (CTX) images. Fan-shaped deposits were classified as being either alluvial fans or putative deltas based on the presence of an arcuate frontal scarp indicative of subaqueous deposition. The fan apex was marked as the location where MOLA-derived contours indicated a transition from convergent to divergent flow, and fan toe defined as the minimum elevation along a profile that extends from the apex to the point along the fan outline that is furthest from the apex. Fan and catchment areas were mapped using CTX images and MOLA-derived topography. Elevation values were obtained from the MOLA Mars Experimental Gridded Data Record (MEDGR) 128 pixel/degree Digital Elevation Model (DEM). Our fans/deltas database has 1468 fans and deltas, 392 outside craters and 1076 inside craters (corresponding to 320 unique fan and/or delta-hosting craters). The largest previous survey involved ≈65 fans (*52*). We excluded 110 "terraced" deltas from further analysis. This is because terraced fans have been hypothesized to result from rapid groundwater outbursts (*31*). We also excluded 560 fans/deltas with fan area < 10 km^2. Without these exclusions, results are similar (Fig. S2). With these exclusions, 854 fans and deltas remained.

565

We corrected both databases for detectability bias (postfluvial resurfacing). A geologic feature of a given relative age has low/no detection probability if the terrain was subsequently resurfaced. To make relative-age assignments, we used the United States Geologic Survey (USGS) Global Geologic Map of Mars (*18*) and also a lower-resolution map by ref. *53* on a 2-pixel-per-degree grid.

570

575

For the valley network-era time slice, terrain not mapped as "Noachian" was masked out. Terrain mapped as "HN" (Hesperian/Noachian), e.g., Meridiani Planum, was also masked out. Based on VN age assignments mapped by ref. *13* as well as more recent geologic mapping (*18*), we removed VNs in these zones: 45-86°E / 45-65°S (Malea Planum), -150 to -86°E / 0-50°N (Alba Patera and high Tharsis), 120-180°E / 11-45°N (Elysium), and 75-97°E / 30-50°S (E. Hellas). This masking removed VNs that crosscut Hesperian or Amazonian terrain; these VNs usually have fewer branches and are usually superposed on young volcanoes. The combination of

these masking steps reduced the number of valley segments from 59419 to 53489. (For legibility, in Fig. 1a we only plot every 4th valley segment). Black dots in Fig. 1a show segments inside our masked-out zone. Most valley segments are part of a larger valley network (n = 9879 of which 9278 survive our masking). When calculating error bars for Fig. 2, we used the $\sqrt{N}$ error associated with the number of valley networks. The location of a point roughly halfway along each valley segment (mean segment length = 12 km) was taken to be representative of the latitude and longitude of that valley segment. Using these coordinates, valley segment elevation was assigned using 8-pixel-per-degree MOLA data (*54*). VNs are greatly underrepresented in Arabia Terra due to erosion, burial, and the inverted-relief preservation style of fluvial materials in this region (e.g. *13*, *27*). Therefore, we excluded from our VN analysis the region where abundant inverted river deposits are found, but few or no river valleys are found (*27*) (Fig. S18). Our conclusions are unaffected by this decision (compare dashed blue line versus solid blue line in Fig. 2). For the analysis of late-stage features, we masked out only terrain mapped by ref. *53* as either "Early Amazonian Vastitas Borealis Unit" or as "Late Hesperian – Late Amazonian volcanic materials".

After masking, in order to make Fig. 2, the non-masked area (km^2) falling into every 2D elevation+latitude bin was calculated (Fig. S4). The number of the corresponding geologic features falling into each 2D bin was calculated. In the case of valley network segments, segment frequencies were weighted by valley segment length. The outputs were marginalized on elevation (for Fig. 2a) or latitude (Fig. 2b). Then the ratio of feature frequency to non-masked terrain area was taken to calculate relative frequency. Finally, the resulting relative frequency histogram was normalized such that the area under each curve was unity (Fig. 2).

Geologic features poleward of 40° in both hemispheres can be obscured by Amazonian slope-softening processes (*55*). Terrain at < −6 km elevation is on the Hellas basin floor, which has enigmatic geology. These limits are shown in Fig. 2 by dotted lines. Our results are robust to the exclusion of these areas.

Debiasing shows that mid-elevation peaks in uncorrected abundance (Fig. S2a) veil trends in debiased frequency that are essentially monotonic: increasing frequency with increasing elevation in the early era, and the opposite trend – increasing frequency with decreasing elevation – later on (Fig. S2a). Debiasing reveals that the late-stage peaks in fluvial-feature abundance at 20°-30° latitude in each hemisphere are equal in amplitude (within error) (Fig. S2a). Debiasing reduces, but does not eliminate, cross-equator asymmetry in VN frequency when plotted as a function of latitude (Fig. 2b). The remaining asymmetry is at least partly explained because high-elevation ancient terrain is rare in the N Hemisphere, and VNs are mostly found at high elevation (Fig. S4). Our inference of latitude-dependent VN formation (Fig. 2b) is supported by independent measurements of valley depth (*56*). Mean valley depth declines from ~140 m within 10° of the equator to ~110 m further (10-30°) from the equator (*56*).

Sensitivity tests for different elevation-assignment choices are shown in Figs. S2-S3. A decline in the elevation of rivers over geologic time is seen regardless of whether we use fan apex elevation, fan toe elevation, or maximum catchment elevation for fans/deltas; and regardless of whether we set the minimum Strahler order for VNs to 1 or 3 (Fig. S3a). Therefore, the detection of a decline in the elevation of rivers over geologic time is robust to different choices about which elevations to plot.

<u>Postfluvial tectonics was likely minor:</u> Mars lacks plate tectonics and the amplitude of post-valley-networks True Polar Wander (TPW) was insufficient to produce the faulting pattern

predicted for TPW (*57*). The pattern of late-stage rivers parallels latitude bands, inconsistent with large-amplitude TPW (Fig. 1b).   The early-stage VNs show a distribution that is roughly sinusoidal with longitude, although this pattern is mostly the result of post-VN resurfacing (gray
630   area in Fig. 1a).

Ref. *15* uses a small-circle-fitting algorithm, applied to the distribution of VNs, to propose a paleopole at 69°N 118°W. However, we applied this algorithm to a synthetic dataset in which, by construction, there is no polar wander, and found roughly the same paleopole (Fig. S6).
635   Specifically, ref. *15* fits a small circle to the observed distribution of valley networks, assuming that the VNs originally formed in a latitude belt that has been distorted by TPW into the observed roughly-sinusoidal shape (Fig. 1a). We applied the same TPW-retrieval procedure to synthetic data in which the distribution of valley networks is spatially uniform – i.e., by construction the synthetic data contain zero evidence for TPW (Fig. S6). Before running the paleopole-retrieval
640   algorithm, we crudely implemented postfluvial resurfacing by removing valleys in areas greatly affected by glacial resurfacing (poleward of 55°), in Arabia Terra (diagonal cut in center of Fig. S6), and in tectonized areas in Acheron and Tempe Terra (affected by faults such as Mareotis and Tempe Fossae). Ref. *15* (their Figure 1) does not show any valleys in Xanthe Terra, or SE of Argyre. For consistency with Figure 1 in (*15*), we also removed valleys in these regions, even
645   though Noachian valleys in Xanthe Terra and SE of Argyre are mapped in ref. *13* (their Figure 1). The paleopole obtained by fitting a small circle to the synthetic data surviving this masking procedure is 79°N 122°W. The VN-based paleopole reported by ref. *15* is 69°N 118°W (Fig. S6). Because these values are similar (Fig. S6), application of the small-circle-fitting procedure of ref. *15* to VN-era geologic data without correcting for subsequent resurfacing is questionable.
650   Therefore, the claim that the VN distribution is evidence for TPW on Mars (*15*) is, likewise, questionable.

Other evidence for post-VN TPW on Mars is also questionable. Although it was once thought that the deviation of putative Mars Northern Ocean shorelines from an equipotential might be evidence
655   for TPW, improved calculations from the same research group show that "Tharsis-induced TPW has a negligible effect" on the deviation of putative Mars Northern Ocean shorelines from an equipotential (*58*). Moreover, putative Mars Northern Ocean shoreline features have been questioned based on high-resolution data (*59*). If half or more of Tharsis was emplaced before the valley networks, then the theoretical upper limit on Tharsis-induced TPW is small, <9° (*58*).
660

The lack of VNs in E. Noachis (around 40°E 30°S) is consistent with ~5° of late-stage TPW, but there is no need to appeal to TPW to explain this local lack of VNs because it can be explained as due to a standing wave in the atmospheric circulation forced by ancient topography (e.g., *60*, and references therein).
665

Despite these concerns, it could be that large-amplitude post-VN TPW did occur on Mars. If post-VN TPW was, in fact, ~20°, then our conclusion that VNs formed at high elevation (Fig. 2a) would be unaffected. In principle, TPW can be directly tested using the orientation distribution of elliptical impact craters (*61*).
670

Light-toned, layered sedimentary rocks: Fig. 2 and Fig. S5 show the distribution of light-toned, layered sedimentary rocks as catalogued by ref. *34*. (For a more inclusive catalog showing a broader distribution of sedimentary rocks, see *62*). The light-toned layered sedimentary rocks catalogued by (*34*) postdate VNs, and both predate and postdate late-stage rivers. Specifically,
675   older light-toned, layered sedimentary rocks (laterally continuous sulfate facies; e.g., Lower Mt. Sharp) are sometimes incised by channels that terminate in small alluvial fans (e.g., *47*).

On the other hand, younger light-toned, layered sedimentary rocks (rhythmite facies; e.g., Upper Mt. Sharp) have never been reported to be incised by fluvial channels. Our detectability mask for light-toned, layered sedimentary rocks is the same as for the late-stage alluvial fans / deltas.

680

3. Global climate model (GCM) simulations.

Surface liquid water requires temperatures above freezing and a supply of H_2O substance (e.g., snowpack or rainfall). On a planet with a very strong greenhouse effect, temperature would not be limiting and surface liquid water would occur wherever H_2O was available. On a planet with a greenhouse effect that was weaker (but still stronger than on modern Mars), liquid water would be found only in the warmest places. In order to confirm and illustrate how patterns of temperature and snowpack stability change with pCO_2, we used the MarsWRF Mars GCM (*17*). MarsWRF is a version of the PlanetWRF GCM (*16*), itself derived from the terrestrial mesoscale WRF model. We ran MarsWRF with horizontal resolution of 5° in both latitude and longitude. The vertical grid uses a modified-σ (terrain-following) coordinate system with 40 vertical resolution levels. Periodic boundary conditions in the horizontal dimensions are employed, and an absorbing ("sponge") upper boundary condition was used. CO_2 radiative transfer uses a correlated-k scheme (*63*). The surface layer flux parameterization scheme is a Monin-Obukhov scheme. We assume pCO_2 is approximately equal to total atmospheric pressure, which is reasonable; Mars' atmosphere is 95% CO_2 today, and atmosphere evolution calculations indicate that was also true in the past. Leading candidate agents of non-CO_2 greenhouse warming (H_2, CH_4, and high-altitude water ice clouds) would increase total atmospheric pressure by <10%. We imposed present-day topography (from MOLA; *54*); spatially uniform surface albedo (0.2) except when (CO_2) ice is on the surface; spatially uniform surface thermal inertia (250 J m^{-2} K^{-1} s$^{-1/2}$); and no atmospheric water cycle nor atmospheric dust. This is because the formation age of the high-elevation, high-albedo, low-thermal-inertia "dust continents" of present-day Mars is unknown and these "dust continent" features might postdate all of the fluvial features in our databases. Mars' geologic record of river forming climates spans 2 Gyr, and almost certainly samples multiple orbital states due to chaotic obliquity variations. Based on previous work (e.g., *64*, and references therein), we selected orbital conditions that were frequently encountered during Mars' chaotic orbital history, and that favor melting (obliquity 35°; eccentricity 0.1; and longitude of perihelion at equinox). The figures show results for 90% of present-day solar luminosity (we also did GCM runs at 75% of present-day solar luminosity). The maximum annually-integrated sublimation potential was calculated using the bare-ground temperature, as the sum of the forced turbulent flux and free turbulent flux, assuming planetary boundary layer relative humidity was small.

The main MarsWRF GCM output is shown in Fig. 3. The potential sublimation rate is defined as the sublimation that would be experienced by snow/ice if that snow/ice were forced to have the same temperature as simulated for bare ground: it is a measure of relative snowpack stability (low potential sublimation rate = greater likelihood of snow accumulation; *65*). Overall, the MarsWRF output is qualitatively consistent with output from the LMD GCM (*9, 65*). GCMs are run for short durations (typically <10 simulated years), due to computational expense, at fixed orbital conditions. Figs. S7-S9 show trends with elevation and latitude. Fig. S7 shows that the surface-temperature lapse rate with surface elevation is steeper at high pCO_2 than low pCO_2. This qualitatively reproduces output from the LMD Mars GCM (*9*). Fig. S8 shows the dependence of the surface temperature on latitude varies with pCO_2. Fig. S9 shows the latitude and elevation dependencies of the potential sublimation rate for high pCO_2 and low pCO_2. Fig. S10 shows more details as well as output for an intermediate pCO_2 (60 mbar).

725

17

Paleo-river distributions almost certainly record multiple orbital states; for example the patterns shown in Fig. 3 are reasonable for explaining the southern mid-latitude belt of alluvial fans, but are unfavorable for alluvial fan formation in the northern midlatitudes (due to the large model-predicted magnitude of potential snow sublimation in the northern midlatitudes).

730

To check the precision of our model, we analyzed the energy conservation properties of our runs. In steady-state, ignoring energy uptake and release by the ground, annually-integrated and planet-averaged absorbed solar radiation equals annually-integrated outgoing longwave radiation. Averaging over the last year of the model run, the 18-mbar run has an energy imbalance of 0.20 W/m^2, the 600-mbar run has an energy imbalance of 2.22 W/m^2, and the 60-mbar run has an energy imbalance of 0.40 W/m^2. This is sufficient for the purposes of our study.

735

4. Survey of the interiors of young craters.

740 <u>Methods.</u> In order to constrain the hydrologic X-ratio (X_H, 20) of late-stage river-forming climates, we surveyed the interiors of ~200 young craters. X_H is approximately equal to the climatic aridity index (AI) in hydrological steady state, if all meltwater/rainwater is routed to the lake, for a closed basin, net of infiltration, and neglecting runoff production on the lake. Our catalog includes deep paleolakes for which X_H constrains annual-average aridity, and also candidate playa deposits, for which X_H might correspond to the wet season. To constrain X_H, we need estimates of paleolake area, A, and drainage area, D ($X_H = D/A - 1$; 20) (Fig. S13).

745

To constrain paleolake area we used flat crater-bottom deposits matching expectations for lake deposits (n=87 including 30 candidates), as well as the elevations of the following features: alluvial fan toes, scarp-fronted deposits interpreted as deltas, and channel-stop elevations (total $n = 126$), internal spillways ($n = 8$), and a candidate shoreline (at Nicholson crater; shown as a blue diamond in Fig. S15; 66) (Fig. S13). The area of a lake deposit is a lower limit on the area of the corresponding lake. For alluvial fan toes and channel termini, we used the elevations of those geologic features to set the elevations of an enclosing contour (Fig. S13). The areas enclosed by these contours are upper limits on A. The slope-break elevation of scarp fronted deposits interpreted as deltas provides a best estimate of past lake level. We recorded only the constraints that (within a given drainage area) were the most hydrologically constraining. Some crater interiors contained multiple drainage areas, due to internal drainage divides.

750

755

760 The interiors of large craters lying wholly within areas mapped as "AHi" (Amazonian and Hesperian impact unit) by ref. 18 were surveyed from 40°S-40°N ($n = 212$ areas; some with >1 large young crater). We also surveyed seven additional large craters (288°E 8°N, 27°E 23°S, 28°E 24°S, 84°E 29°S, 83°E 30°S, 83.7°E 29.8°S, 74.2°E 23.0°S) that have relatively well-preserved rims, demonstrating relative youth. To search for paleohydrologic proxies, we used CTX (Context Camera) data (67), supplemented by HiRISE (High Resolution Imaging Science Experiment) (68) images. For topography at most sites, we used Mars Orbiter Laser Altimeter (MOLA) Precision Experimental Data Records (PEDRs) (54), supplemented in some places by MOLA gridded data and CTX Digital Terrain Mmodels (available at https://uchicago.app.box.com/s/bcpp75knzo6tp2ijk4uffop8wjbk117n).

765

770

Each of the proxy types that we use in our global survey have been described previously (e.g., 3, 69). For example, flat-lying sediments interpreted as lake deposits have been intensively described at Holden crater by ref. 70. As far as we know, this is the first global survey for flat crater-bottom deposits that we interpret as lake deposits, so we describe this specific proxy type below. Flat crater-bottom deposits (FCBDs) frequently have slopes of 1 part in 1000, a factor of 10-20 flatter than nearby alluvial fans. FCBDs lack channels, appear densely cratered, show pits

775

and grooves due to wind erosion, are usually found downslope from alluvial fans, and are typically bounded by outward-facing scarps (Fig. S14). Internal layering and susceptibility to wind erosion show that these are indurated sedimentary deposits. Extreme flatness and location at the bottom of a crater indicate that aggradation was controlled by an equipotential, most likely surface liquid water. Possible cementing agents for FCBDs include chlorides or iron oxides. FCBDs are unlikely to be pure salt deposits, for example because analysis of salty deposits on Mars always shows a major proportion of siliciclastic material. Siliciclastic material could be transported by runoff from the crater sidewalls, or it could be blown in by the wind. In some cases, sinuous ridges that we interpret as capped by fluvial deposits connect to FCBDs (this association has been previously reported by ref. *71*). When CTX/HiRISE morphology indicated an FCBD but topographic data were lacking, we marked the deposit as a "candidate" FCBD (open blue triangles in Fig. S15).

More time is needed to build up a fan than is required to carve a channel. Therefore, the X_H obtained from setting lake elevation equal to a channel-stop elevation (requiring that the lake level did not exceed the channel stop elevation for at least as long as it took to carve the channel) is a less stringent constraint on lake level than that obtained from a fan toe elevation. In Fig. S15, we mark channel-stop constraints on X_H with red open triangles, and fan toe X_H constraints with red filled triangles.

The frequency with latitude of evidence for past rivers/lakes (Fig. S16), normalized by the number of "AHi" craters, shows peaks at 20-40°S and 20-40°N, and a smaller peak at 10°S-10°N, defining local minima at 10-20°N and at 10-20°S (Fig. S16). This is consistent with the latitudinal distribution of fan/delta frequency in our much larger (overlapping) catalog of alluvial fans/deltas (Fig. 2b).

Our approach treats the present-day topographic relationships between lake deposit outcrops and alluvial fan deposit outcrops as being representative of the topographic relationships between those deposits when the rivers were flowing. This is usually an acceptable approximation, even though lake deposit extent will wax and wane with stratigraphic elevation. Occasionally (at Saheki crater, at the large crater SE of Saheki, and at 323°E 18°S), we observed flat crater-bottom deposits topographically above fan toes. We interpret this as showing that wind erosion has (locally) cut more deeply into the fan deposits than into the playa deposits. At Saheki crater, we observed the transition between an alluvial fan and a flat crater-bottom deposit interpreted as a lake or playa deposit. The elevation contour corresponding to this transition corresponds to our best estimate of paleolake extent (shown as a blue diamond in Fig. S15).

<u>Details of Aridity Results.</u> Typical X_H from our late-stage survey was 7-38 (median fan toe constraint to median lake deposit constraint), corresponding to arid-to-hyperarid conditions, with deltas and overspill channels recording semi-arid conditions (median $X_H = 4$). This is more arid than the aridity typically reported for early lakes ($X_{H,ancient} = 5\pm2$, e.g., *20*), but this aridification was not uniform with crater size or elevation/latitude.

Fig. S15a shows that bigger craters were not any drier than small craters (there is a weak trend to bigger craters being wetter). This argues against very brief wet events, for the following reason. Let the energetic upper limit on evaporation E be E_{max}. For a given lake, if we know lake extent A, catchment extent D, and also know the paleotopography, then we know the minimum total runoff production P_{tot}. If the wet event was very brief (short τ), then $P_{tot}/\tau \gg E_{max}$. But if $P_{tot}/\tau \gg E_{max}$, then during a wet event small craters would fill up more than big craters. That is in contradiction to the observations. For fiducial values of $E_{max} = 1$ m/yr (*2*) and $P_{tot} = 30$ m, each wet event must have lasted at least decades.

This result can also be understood as follows. Brief intense runoff production events (e.g., top-down melting, rain-on-snow) predict higher X_H for bigger craters because small sinks fill quicker than big sinks. Approximate a lake with volume V as an inverted cone, $V = \frac{1}{3} \pi R_{lake}^2 h$, where h is lake depth. We suppose that crater floors have the same floor slope s, so $V = \frac{1}{3} s \pi R_{lake}^3$. Considering a range of craters with different sizes, for uniform runoff production $V \propto R_{crater}^2$. Thus $R_{lake} \propto R_{crater}^{2/3} \rightarrow (R_{lake} / R_{crater}) \propto R_{crater}^{-1/3}$. Since for a closed basin $X_H \propto (R_{lake} / R_{crater})^2$, $X_H \propto R_{crater}^{2/3}$. Contrary to this prediction, we observe that X_H is negatively correlated with R_{crater} ($p \leq 0.004$) (Fig. S15a). For example, delta-top elevations suggest lower X_H for larger craters. These observations disfavor the brief-pulse hypothesis.

Overall, brief intense runoff production events (e.g., top-down melting, rain-on-snow) predict a more random pattern of aridity than is observed. Because late-stage climate-fed lakes were (at least in some places) deep (e.g. 0.7 km; *72*), a brief pulse would require large energy inputs, greatly in excess of insolation, to either melt snow or power rainstorms. Because the required energy input is greatly in excess of insolation, runoff production in this short-pulse scenario would be relatively insensitive to latitude and elevation. Contrary to the predictions of the brief-pulse model, we observe that X_H is sensitive to latitude and elevation (Fig. S15b/S15c). We find that paleolakes at >-1500m elevation record more arid climates than at <-1500m ($p=0.04$), with $X_H < 10$ found mostly at low elevation ($p = 0.01$) (SM) (Fig. S15). This trend might reflect the effect of latitudinal gradients in elevation on global atmospheric circulation and/or the water cycle ($X_H < 10$ is less common south of 10°S; $p = 0.002$, SM), (SM). Elevation control on late-stage paleolake levels (i.e., elevation control on X_H) is consistent with elevation control on late-stage river abundance (Figs. 1-2).

To see if the X_H trends could be an artifact from shot-noise (random) error, we used two approaches. This analysis is informal and geologic prior knowledge / judgment affects our choices. (Systematic errors are more important than random error in our analysis.) In the first approach, we defined a "hard constraint" to exclude channel-stops, candidate lake deposits, and basins where data permit X_H on both sides of $X_H = 10$. (This is conservative in that the channel-stops are probably good paleohydrologic constraints). This leaves 46 data points. We counted the number of hard constraints falling into rectangular regions in the plots in Fig. S15. The data are not evenly distributed between the rectangular regions (bold numbers in Fig. S15). To find the probability that the trends resulted from chance, we resampled-with-replacement from the hard-constraint occurrences. We assessed trend agreement by comparing the sum of the number of resampled data points in diagonally adjacent rectangles to the sum of data in the orthogonal pair of diagonally-adjacent rectangles. This resampling showed $p = 0.0017$ for the latitude trend, $p = 0.0034$ for the crater-diameter trend, and $p = 0.013$ for the elevation trend. As a second approach to uncertainty quantification, we randomly sampled aridities from a log-uniform prior on $X_H = \{0.1, 10^4\}$, clipped on a per-basin basis to satisfy the geologic constraints. (We did not resample basin occurrence in this approach, only the uncertainty on X_H within each basin). This approach uses all the data (221 measurements, 118 basins), including channel-stops and candidate lake deposits. Kernel density estimates obtained from this approach are shown in Fig. S17. For each bootstrapped ensemble of basin aridities, we calculated the number of bootstrapped data falling into the rectangular regions shown in Fig. S15. Then, as for the first approach, we assessed trend agreement by comparing the sum of the number of resampled data points in diagonally adjacent rectangles to the sum of data in the orthogonal pair of diagonally-adjacent rectangles. From 10^4 bootstraps, we find that that in all cases the latitudinal trend in the deterministic approach is recovered (lower X_H at latitudes S of 10°S), in all cases the crater-diameter trend in the

deterministic approach is recovered (lower X_H for crater diameter > 60 km), and in 9608 cases the elevation trend is recovered (lower X_H at elevations < -1500m). We did a sensitivity test on these results using a different log-uniform prior, $X_H = \{0.1, 10^{14}\}$. The sensitivity test results were unchanged for the latitude trend and crater-diameter trend, and trend recovery increased to 9817/1000 for the elevation trend.
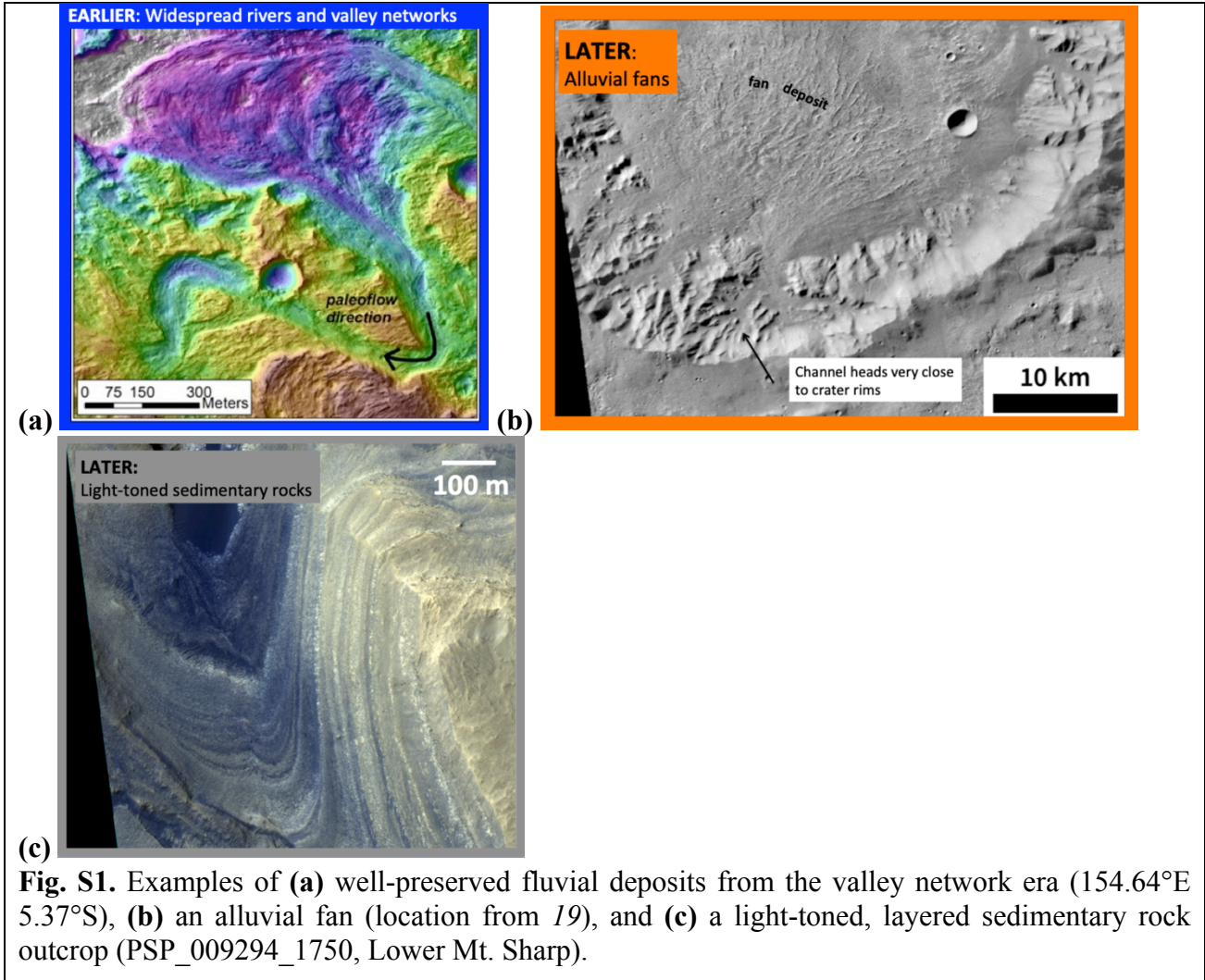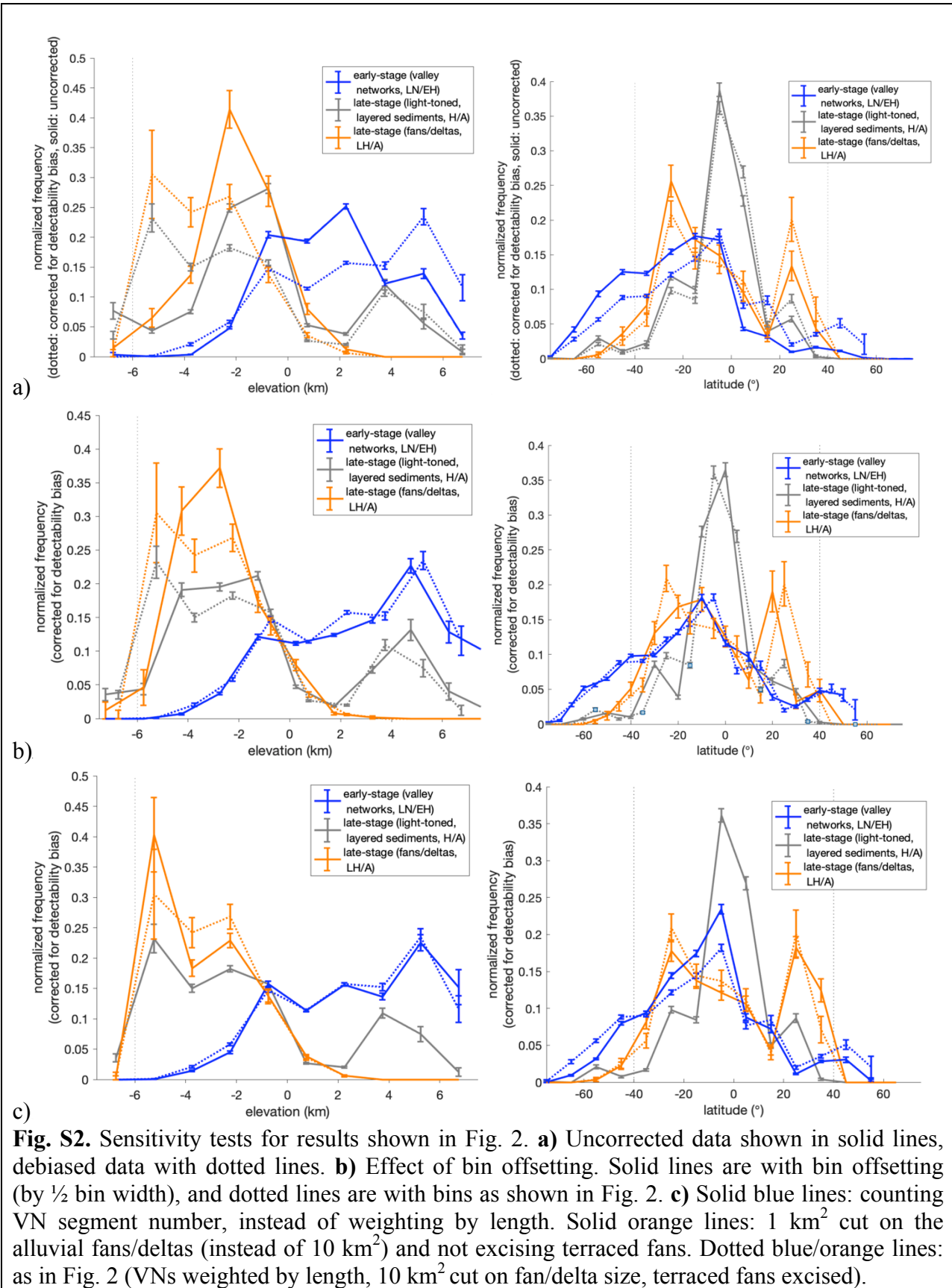
Supplementary Figures.

Fig. S1. Examples of **(a)** well-preserved fluvial deposits from the valley network era (154.64°E 5.37°S), **(b)** an alluvial fan (location from *19*), and **(c)** a light-toned, layered sedimentary rock outcrop (PSP_009294_1750, Lower Mt. Sharp).
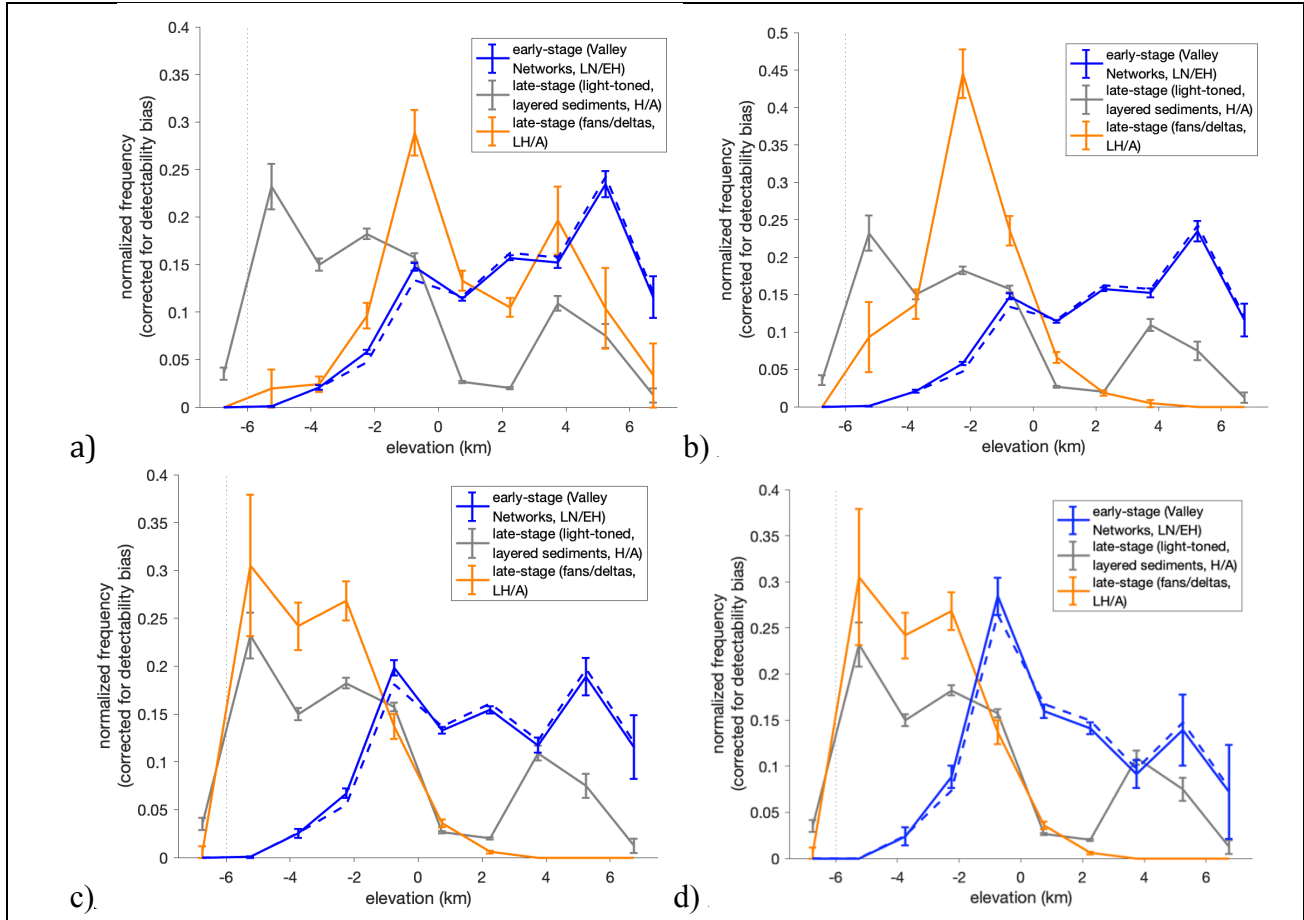
885

Fig. S2. Sensitivity tests for results shown in Fig. 2. **a)** Uncorrected data shown in solid lines, debiased data with dotted lines. **b)** Effect of bin offsetting. Solid lines are with bin offsetting (by ½ bin width), and dotted lines are with bins as shown in Fig. 2. **c)** Solid blue lines: counting VN segment number, instead of weighting by length. Solid orange lines: 1 km^2 cut on the alluvial fans/deltas (instead of 10 km^2) and not excising terraced fans. Dotted blue/orange lines: as in Fig. 2 (VNs weighted by length, 10 km^2 cut on fan/delta size, terraced fans excised).

Fig. S3. Further sensitivity tests for elevation trends over time. **(a)** maximum elevation within catchment for fans/deltas, vs. elevation of valley-network valleys of all Strahler orders (this is not an apples-to-apples comparison, as catchment maximum elevation will overstate the elevation of typical channel heads): **(b)** fan apex elevation vs. elevation of valley-network valleys of all Strahler-orders: **(c)** fan toe elevation vs. elevation of valley-network valleys of Strahler orders 2 and higher ("trunk" streams): **(d)** fan toe elevation vs. Strahler orders 3 and higher.
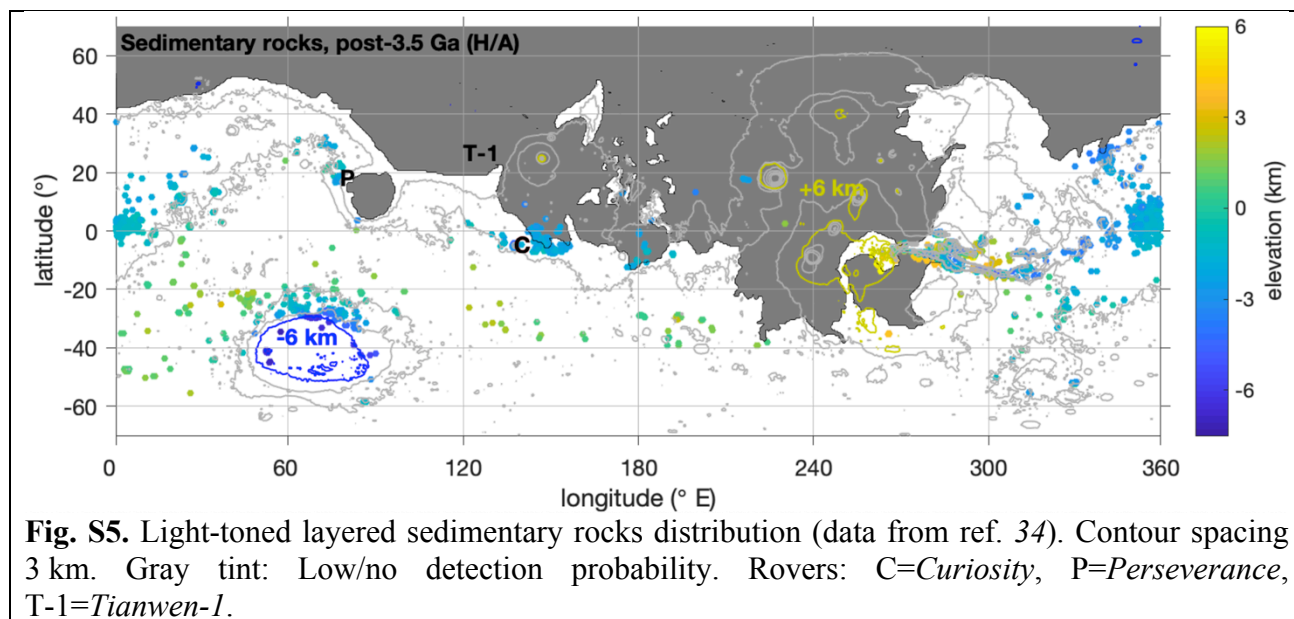
890
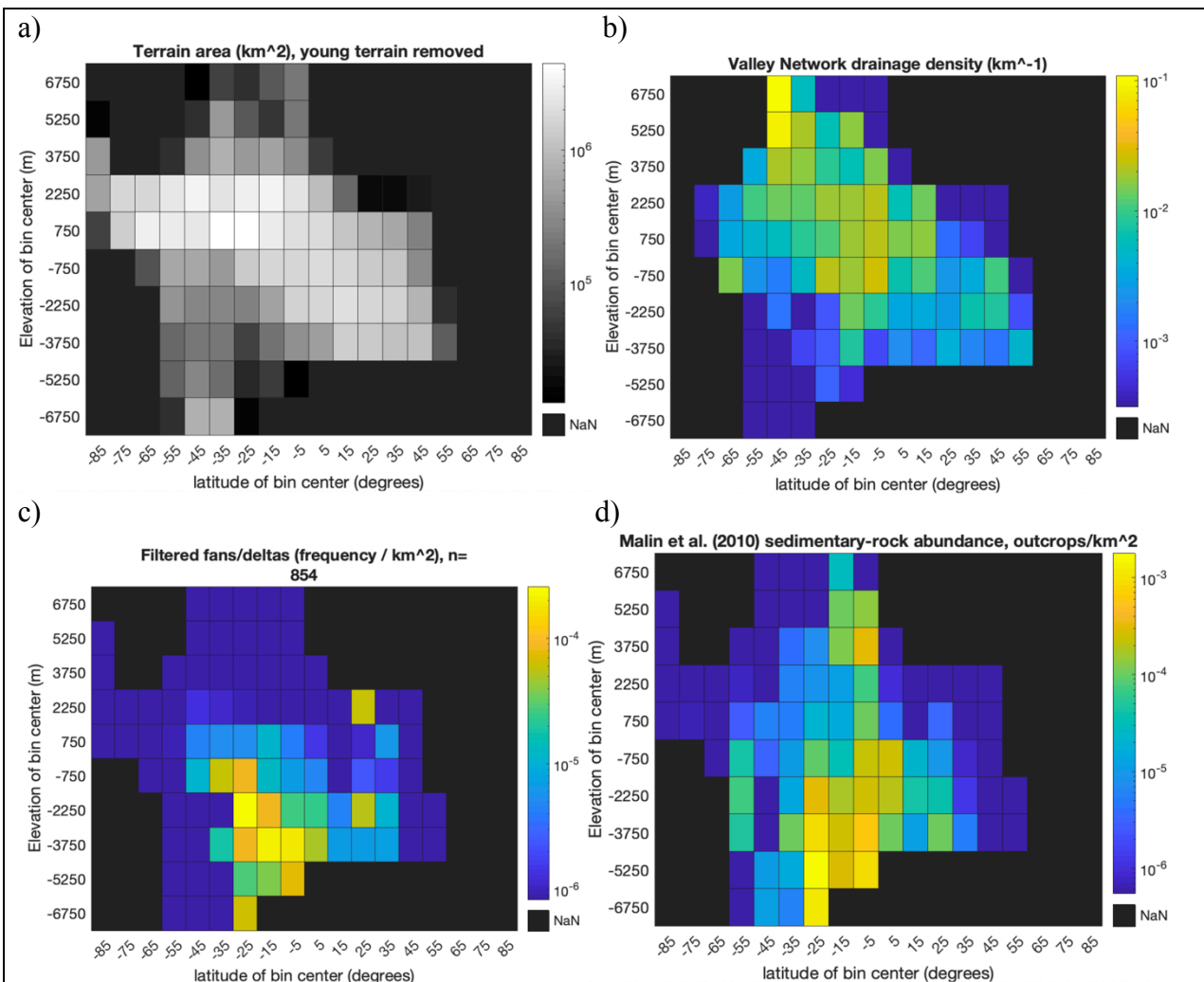
Fig. S4. Elevation+latitude distribution of (a) non-young terrain (Fig. 1b mask), (b) valley networks, (c) alluvial fans/deltas, and (d) light-toned, layered sedimentary rocks. Late stage latitude control is not an artifact of latitude-dependent asymmetry. For this figure only, elevation+latitude pixels with area $< 10^4$ km^2 are not shown (as they tend to be statistically noisy).

Fig. S5. Light-toned layered sedimentary rocks distribution (data from ref. *34*). Contour spacing 3 km. Gray tint: Low/no detection probability. Rovers: C=*Curiosity*, P=*Perseverance*, T-1=*Tianwen-1*.
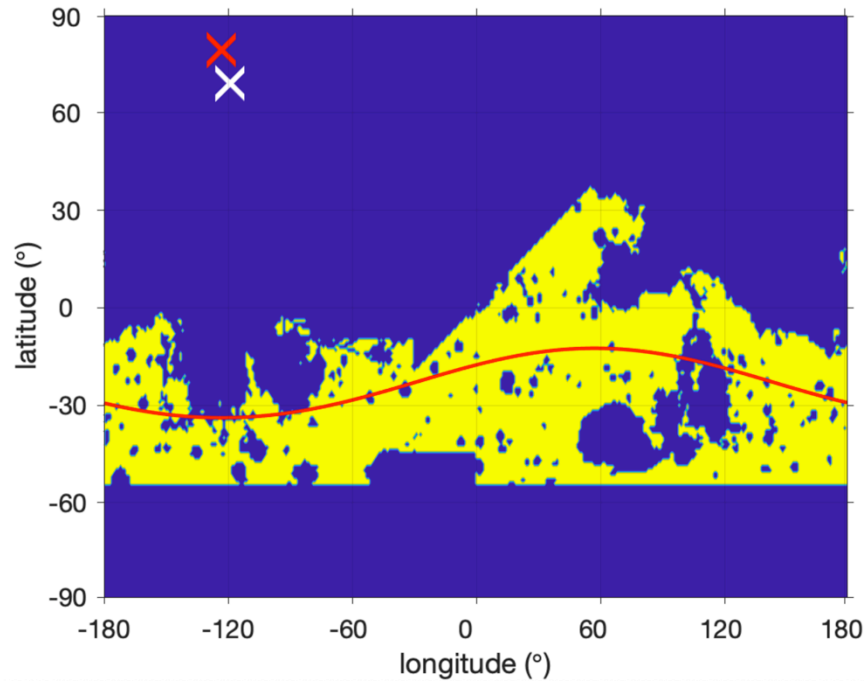
895

Fig. S6. Example of how a small-circle-fitting pipeline can lead to a detection of TPW when no TPW has occurred. We used a synthetic dataset in which, by construction, there is zero evidence for TPW (a uniform distribution). The resulting distribution of valley networks is shown in yellow and the resurfacing mask in blue. The red line shows the small circle that is the best fit to the yellow distribution, the corresponding best-fit (spurious) paleopole is shown by the red cross, and the paleopole reported by (*15*) based on VN distribution is shown by the white cross.
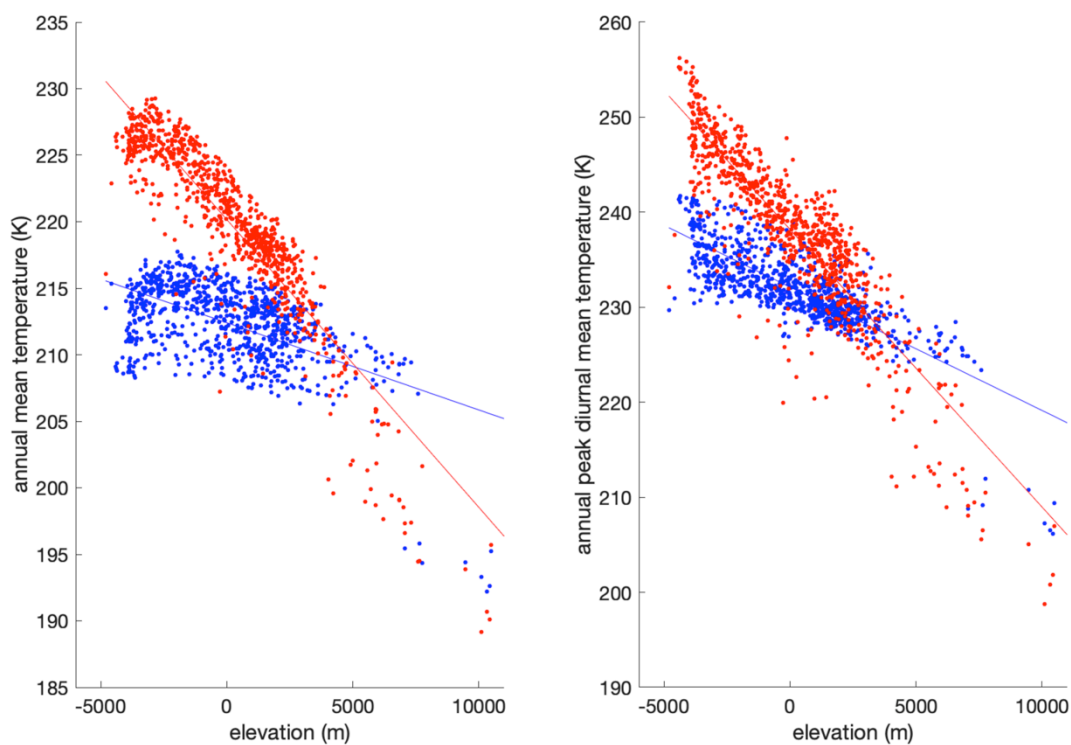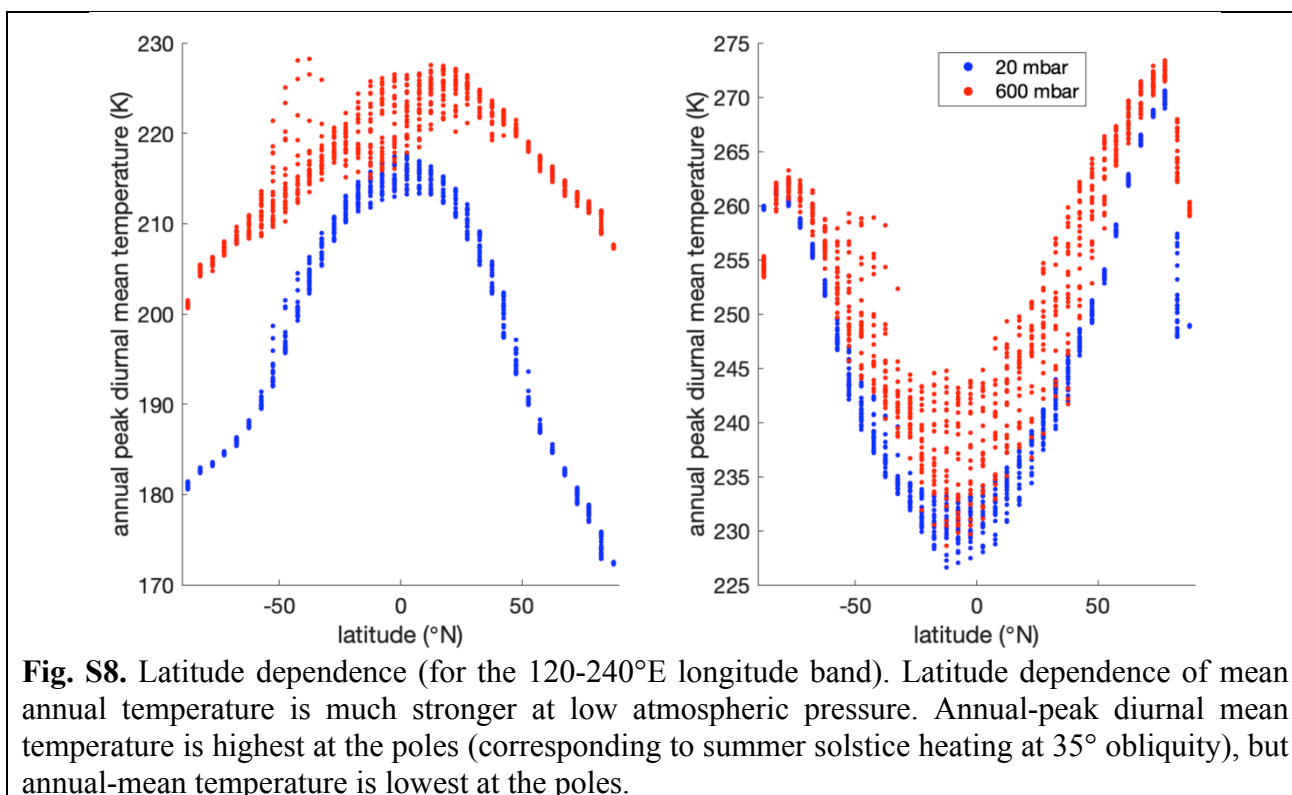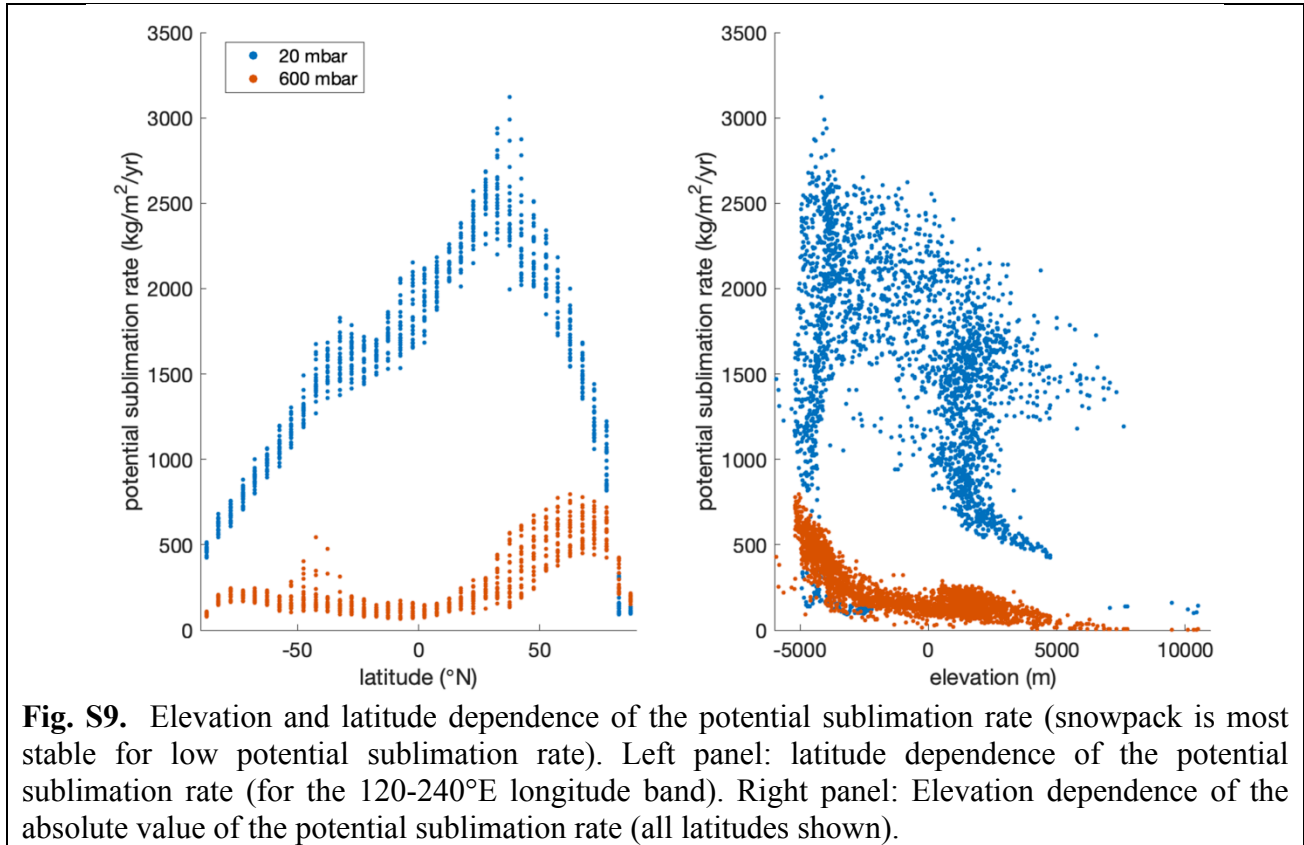
Fig. S7. Elevation dependence (for +/-30° latitude band in order to minimize the effects of seasonal CO_2 ice). Red points are different spatial locations for 600 mbar simulation, blue points are different spatial locations for 20 mbar simulation. One model output point (corresponding to the summit of Olympus Mons) is clipped out.
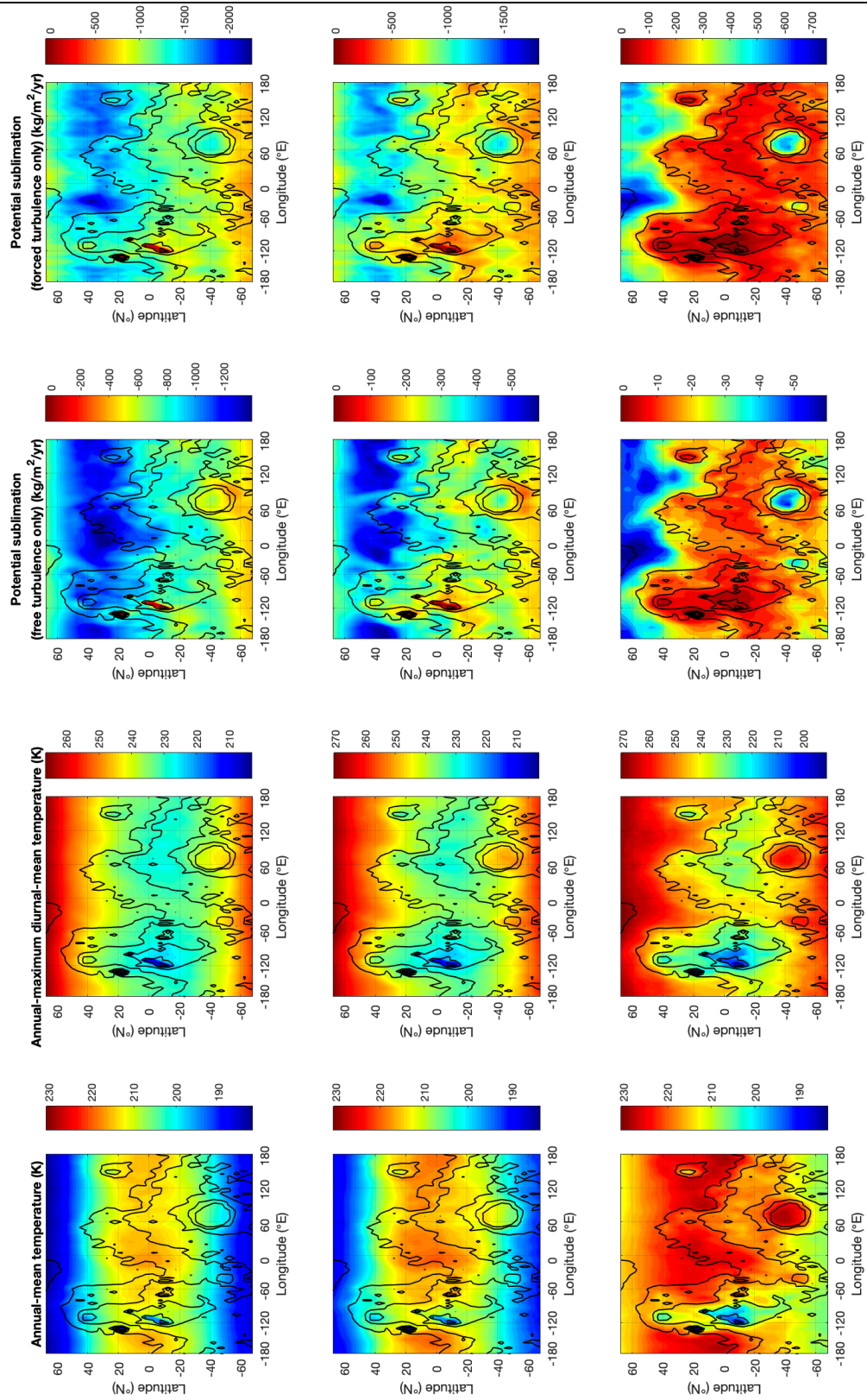
900

Fig. S8. Latitude dependence (for the 120-240°E longitude band). Latitude dependence of mean annual temperature is much stronger at low atmospheric pressure. Annual-peak diurnal mean temperature is highest at the poles (corresponding to summer solstice heating at 35° obliquity), but annual-mean temperature is lowest at the poles.

Fig. S9. Elevation and latitude dependence of the potential sublimation rate (snowpack is most stable for low potential sublimation rate). Left panel: latitude dependence of the potential sublimation rate (for the 120-240°E longitude band). Right panel: Elevation dependence of the absolute value of the potential sublimation rate (all latitudes shown).

905

Fig. S10. Global climate model output. Left column: 20 mbar pCO$_2$. Center column: 60 mbar pCO$_2$. Right column: 600 mbar pCO$_2$. Contour interval 3 km, lowest contour at -5 km. For sublimation maps, warm colors are more favorable for snow accumulation.
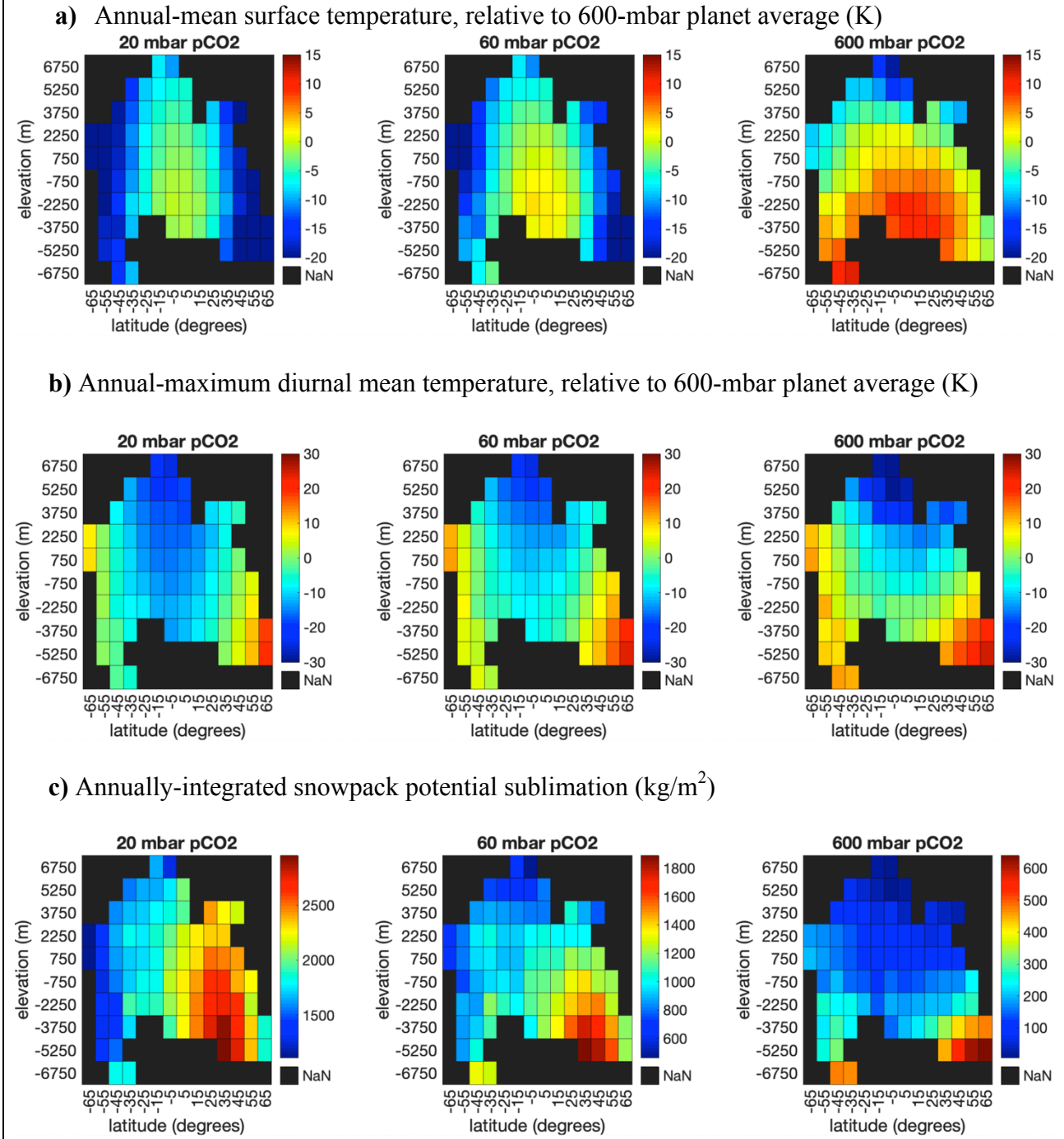
a) Annual-mean surface temperature, relative to 600-mbar planet average (K)

b) Annual-maximum diurnal mean temperature, relative to 600-mbar planet average (K)

c) Annually-integrated snowpack potential sublimation (kg/m^2)

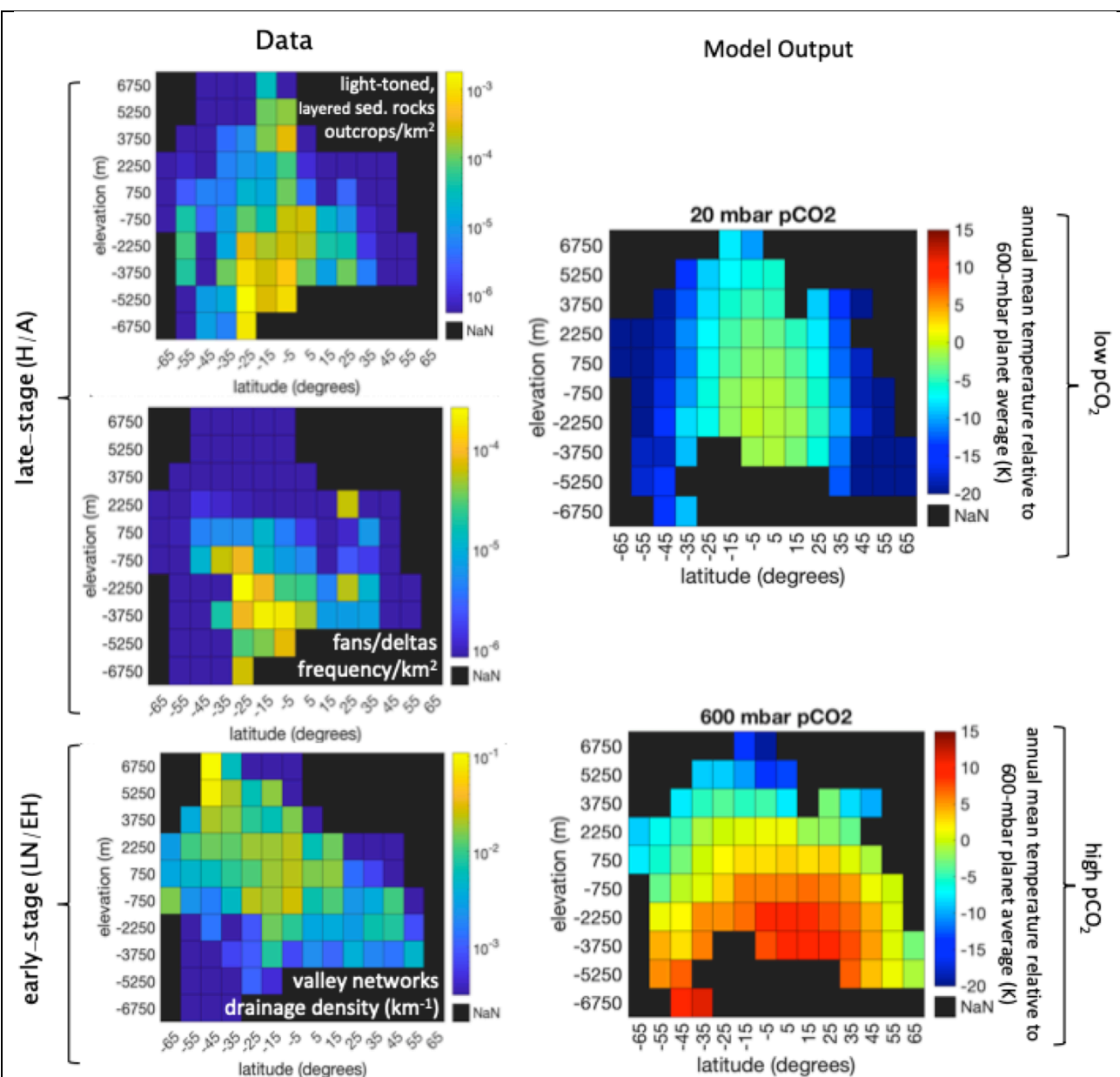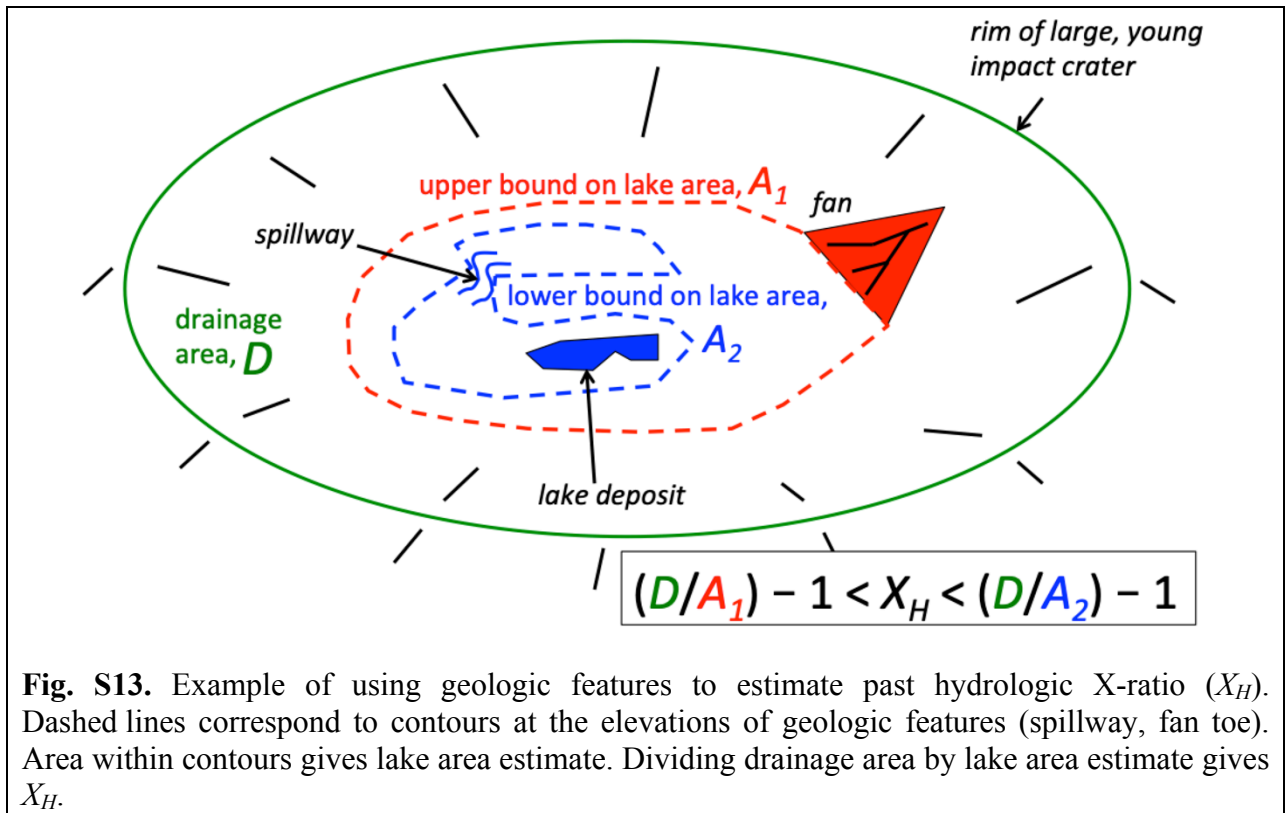**Fig. S11.** Elevation and latitude distribution of GCM output. The average value of GCM pixels is shown.

Fig. S12. Data-model comparison. (*Left column:*) The distribution of liquid-water requiring geologic features shows a shift from an early-stage high-elevation preference (with secondary latitude control) to late-stage latitude control with low-elevation preference. (*Right column:*) GCM output confirms previous reports (*9*) that the mean temperature pattern is controlled by elevation (and secondarily latitude) at high pCO_2, with much stronger latitude control at low pCO_2.

910

Fig. S13. Example of using geologic features to estimate past hydrologic X-ratio (X_H). Dashed lines correspond to contours at the elevations of geologic features (spillway, fan toe). Area within contours gives lake area estimate. Dividing drainage area by lake area estimate gives X_H.
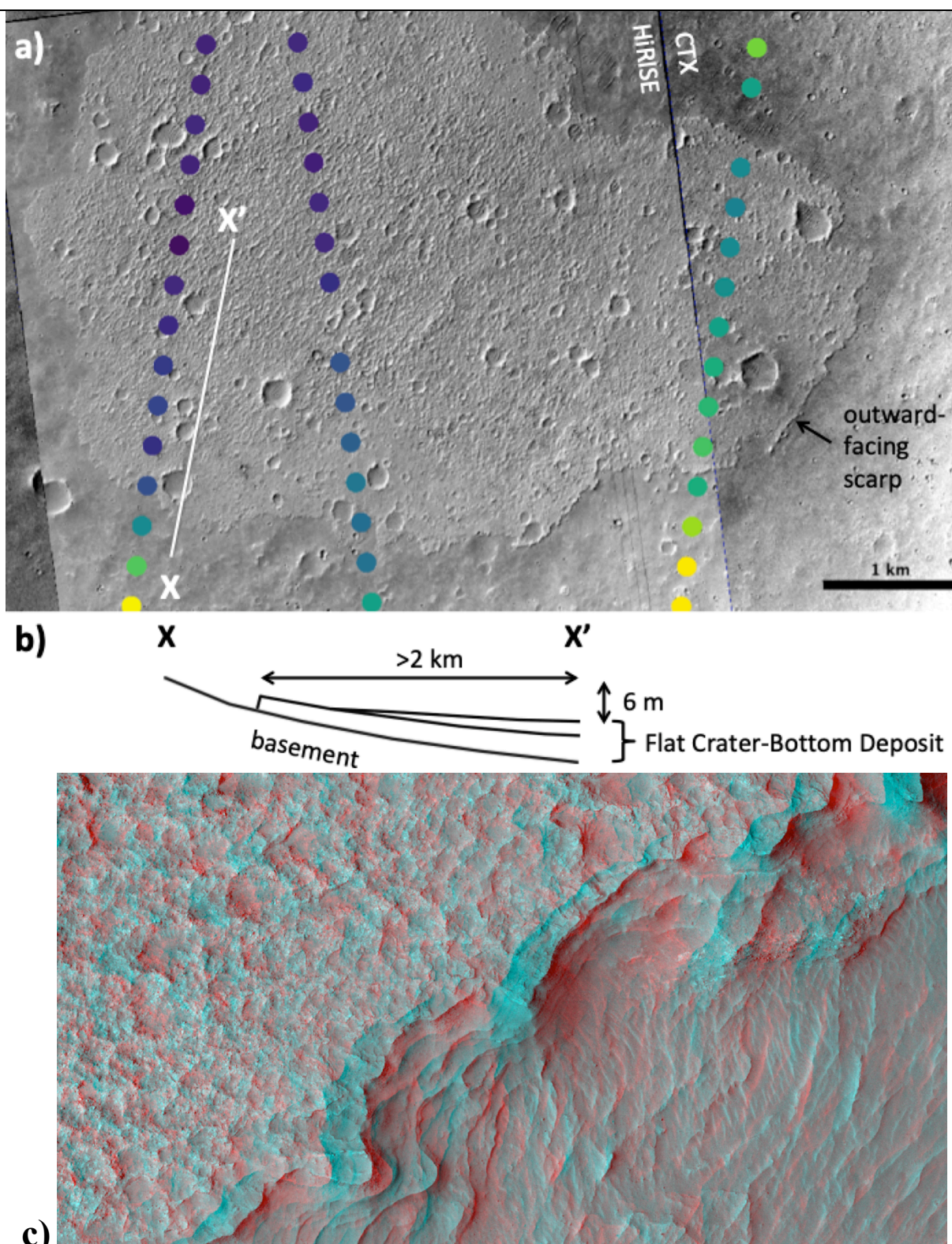
Fig. S14. (a) Example of a flat crater-bottom deposit (interpreted as a lake deposit). Area of HiRiSE image ESP_062496_1880 (8.0°N 287.8°E). Color scale corresponds to laser altimeter data and runs from -180 m (yellow) to -220 m (deep blue). **(b)** Sketch cross-section of profile X-X' in (a). **(c)** Red-blue anaglyph of the margin of a flat crater-bottom deposit (HiRiSE stereopair ESP_065480_1495 ESP_065414_1495), showing nearly-horizontal mid-toned layers exposed beneath the lighter-toned erosionally-resistant cap. Image is 920 m across.
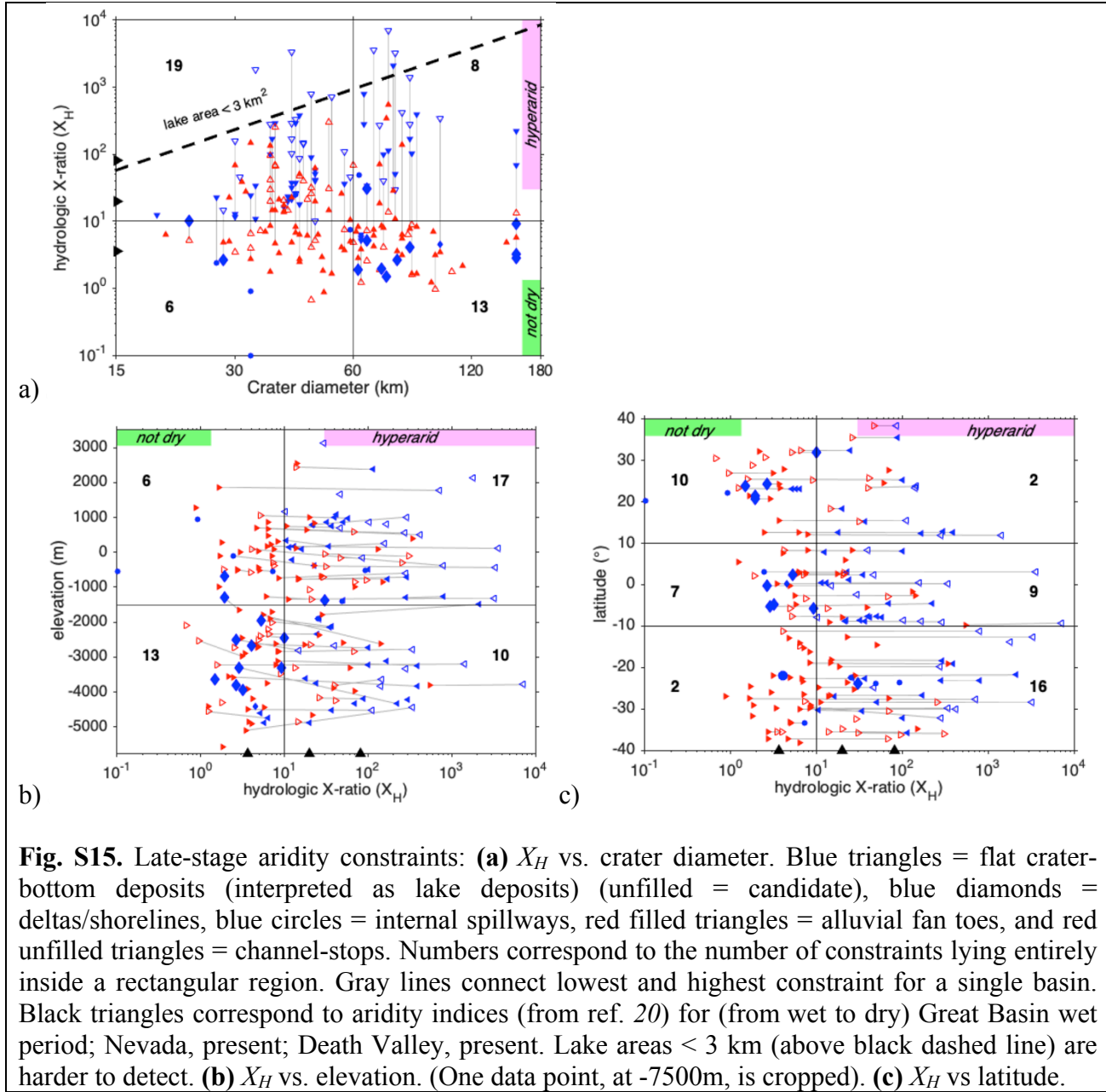
Fig. S15. Late-stage aridity constraints: **(a)** X_H vs. crater diameter. Blue triangles = flat crater-bottom deposits (interpreted as lake deposits) (unfilled = candidate), blue diamonds = deltas/shorelines, blue circles = internal spillways, red filled triangles = alluvial fan toes, and red unfilled triangles = channel-stops. Numbers correspond to the number of constraints lying entirely inside a rectangular region. Gray lines connect lowest and highest constraint for a single basin. Black triangles correspond to aridity indices (from ref. *20*) for (from wet to dry) Great Basin wet period; Nevada, present; Death Valley, present. Lake areas < 3 km (above black dashed line) are harder to detect. **(b)** X_H vs. elevation. (One data point, at -7500m, is cropped). **(c)** X_H vs latitude.
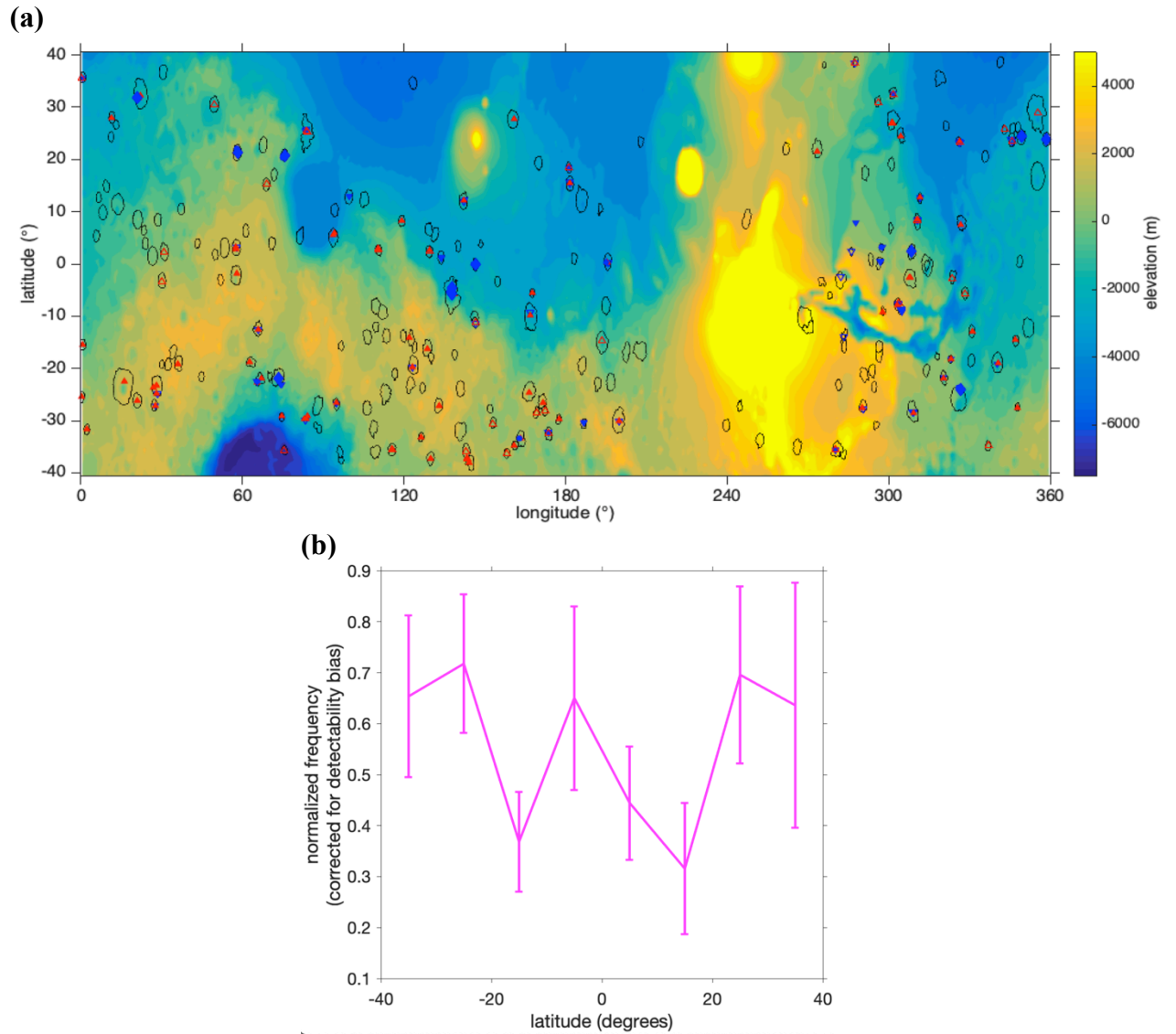
915

Fig. S16. (a) Aridity survey map. Black contours outline the geologic units from (*18*) corresponding to large young impact craters inspected for paleohydrology constraints. Blue triangles = flat crater-bottom deposits (interpreted as lake deposits) (unfilled = candidate), blue diamonds = deltas/shorelines, blue circles = internal spillways, red filled triangles = alluvial fan toes, red unfilled triangles = channel-stops. **(b)** Distribution of craters with paleohydrologic evidence with latitude (expressed as a fraction of the number of surveyed craters in that latitude band).
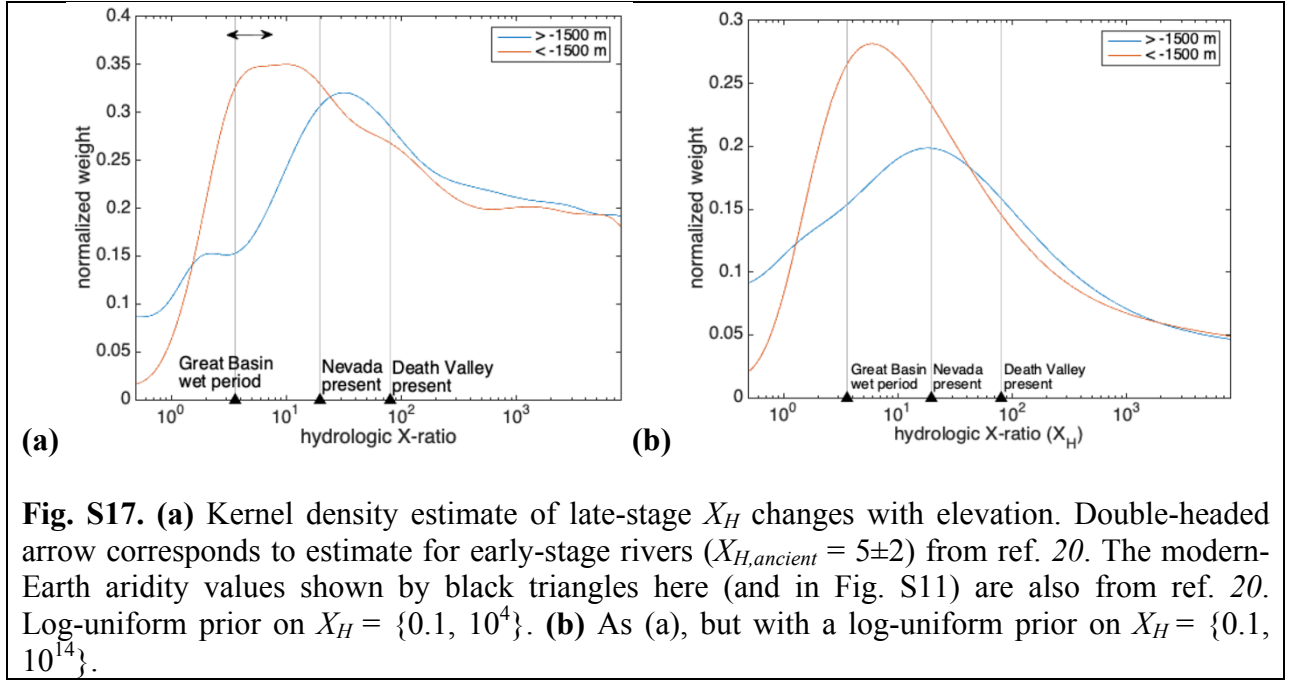
(a)

(b)

Fig. S17. (a) Kernel density estimate of late-stage X_H changes with elevation. Double-headed arrow corresponds to estimate for early-stage rivers ($X_{H,ancient}$ = 5±2) from ref. *20*. The modern-Earth aridity values shown by black triangles here (and in Fig. S11) are also from ref. *20*. Log-uniform prior on X_H = {0.1, 10^4}. **(b)** As (a), but with a log-uniform prior on X_H = {0.1, 10^{14}}.
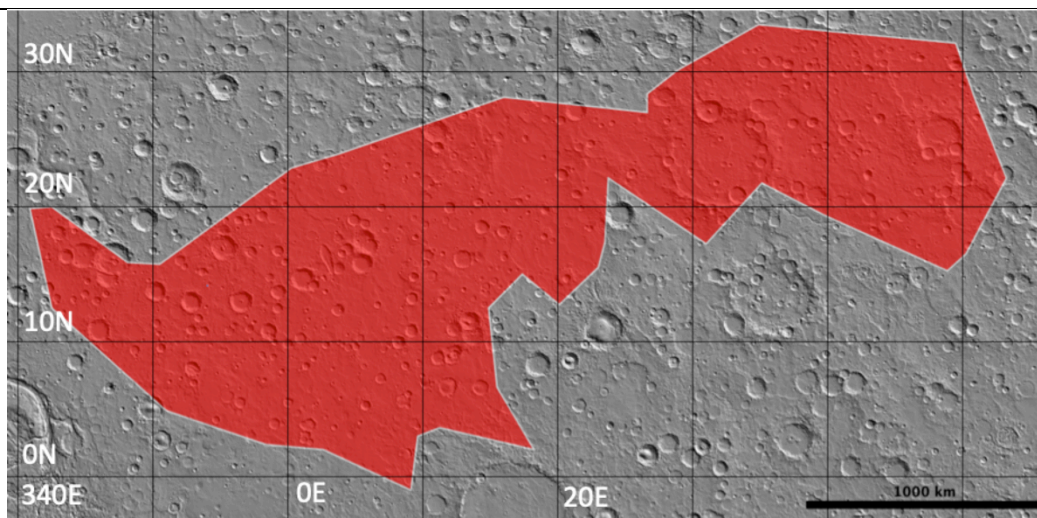
920

Fig. S18. Arabia Terra mask for excluding region of low/no preservation potential for valley networks, guided by the inverted-channel map of ref. *27* (their Fig. S1).

Location	Evidence (pre-fluviolacustrine-sed or syn-fluviolacustrine-sed impact craters internal to "AHi" impact rims as mapped by ref. 18) (ø = diameter)	Main-crater diam. (km)	Estimate [*] of Time Gap
83°E 30°S (Nako)	Rivers/lakes activity postdate ejecta from ø = 40 km crater to the E → long time gap	43	At least Gyr
167°E 10°S (Reuyl)	ø = 6 km crater on SW side contains fan.	86	0.4 Gyr
303.5°E 7.6°S	ø = 2 km crater inside large crater (on W side) has inlet breach or alcove.	45	0.2 Gyr
311°E 8°N	Contains ø = 11 km crater that has alcoves, fans, and a possible lake deposit.	68	0.2 Gyr
326°E 23°N (Wahoo)	Material with lineations perpendicular to high relief grades into wind-eroded material that is itself embayed by smoother, ramp material with much less wind erosion. Channel also postdates wind erosion.	67	At least Myr (to allow time for wind erosion)
84°E 25.4°N (Peridier)	ø = 9 km crater on NW side is prefluvial.	100	0.6 Gyr
22°E 32°N (Cerulli)	Channel crosscuts ø = 7 km crater on the SW rim.	130	0.2 Gyr
144°E 38°S	Exit breach on ø = 2km crater on E side (internal to main crater).	47	0.2 Gyr
187°E 30°S	FCBD postdates ejecta from ø = 10 km crater on E rim (which itself contains an FCBD).	31	6.5 Gyr (sic)
297.5°E 3°N	Inlaid ø = 4 km crater inside W rim has exit breach into main crater.	27	2 Gyr
280°E 36°S	Probable exit-breach crater (ø = 6 km), inside N rim.	69	0.6 Gyr
326°E 26°S (Holden)	Previously documented (2, 19).	154	At least Myr
19 sites (14 craters)	Interbedded craters. From ref. 19.	Varies between sites.	>(100–300) Myr

925

930

Note. [*] Best-estimate time gap assuming modern impact flux (valid for the Amazonian, too low by a factor of 3.2 at 3.5 Ga) and the Hartmann chronology, using the nearest bin in the tables of ref. 49. Assuming the count area for detection of interbedded craters is the entire crater (which will greatly understate the true time gap), and dividing results by a factor of 20 to take account of the fact that we only found interbedded craters in 12 of the ~219 craters that we surveyed. In reality synsedimentary and presedimentary impact craters are usually detected at or near the perimeter of sedimentary deposits, so the survey area is smaller than assumed here. Thus these estimates are likely biased low; even so, the timescales are long.

Table S1. Evidence against a localized impact trigger for late-stage rivers and lakes.

Supplementary Data: JMARS-readable ESRI. shp shapefiles.